Available online at www.sciencedirect.com
ScienceDirect
Comput. Methods Appl. Mech. Engrg. 279 (2014) 579–605
Computer methods in applied mechanics and engineering
www.elsevier.com/locate/cma

Variational multi-scale stabilized formulations for the stationary three-field incompressible viscoelastic flow problem

Ernesto Castillo, Ramon Codina*

Universitat Politècnica de Catalunya, Jordi Girona 1-3, Edifici C1, 08034, Barcelona, Spain

Received 12 April 2014; received in revised form 26 June 2014; accepted 5 July 2014
Available online 14 July 2014

Abstract

In this paper, three-field finite element stabilized formulations are proposed for the numerical solution of incompressible viscoelastic flows. These methods allow one to use equal interpolation for the problem unknowns $\boldsymbol{\sigma}$–$\boldsymbol{u}$–p (elastic deviatoric stress–velocity–pressure) and to stabilize dominant convective terms. Starting from residual-based stabilized formulations, the proposed method introduces a term-by-term stabilization which is shown to have a superior behavior when there are stress singularities. A general discontinuity-capturing technique for the elastic stress component is also proposed, which allows one to eliminate the local oscillations that can appear when the Weissenberg number We is high and the fluid flow finds an abrupt change in the geometry. The formulations are tested in the classical 4:1 planar contraction benchmark up to $\mathrm{We} = 5$ in the inertial case, with Reynolds number $\mathrm{Re} = 1$, and up to $\mathrm{We} = 6.5$ in the quasi non-inertial case, with $\mathrm{Re} = 0.01$. The standard Oldroyd-B constitutive model is used for the rheological behavior and linear and quadratic elements for the spatial approximation.

Keywords: Viscoelastic fluids; Stabilized finite element methods; Oldroyd-B fluid; Discontinuity capturing technique

1. Introduction

The finite element approximation of the flow of viscoelastic fluids presents several numerical difficulties. It inherits obviously the problems associated with the approximation of the incompressible Navier–Stokes equations, mainly the compatibility between the velocity–pressure approximation and the treatment of the nonlinear advective term. But, on top of that, now the constitutive equation is highly nonlinear, with an advective term that may lead to both global and local oscillations in the numerical approximation. Moreover, even in the case of smooth solutions it is necessary to meet some additional compatibility conditions between the velocity and the stress interpolation in order to control velocity gradients. Elements that satisfy the compatibility requirements velocity–pressure and stress–velocity are rare.

The treatment of the nonlinearity is another aspect that deserves to be studied in detail. Apart from the nonlinearity in the convective term of the momentum equation, the constitutive equation has two additional nonlinear terms,

* Corresponding author. Tel.: +34 934016486.
E-mail addresses: ecastillo@cimne.upc.edu (E. Castillo), ramon.codina@upc.edu (R. Codina).

http://dx.doi.org/10.1016/j.cma.2014.07.006
0045-7825/

namely, the convective one and the rotational one. Fixed point type schemes are robust, but with a very low convergence rate when the elastic component increases [1]. Newton–Raphson schemes are most extensively used in the literature [2,3], although they often need to be complemented with additional numerical tools, such as continuation methods and relaxation schemes. The results obtained in this work have been obtained using the Newton–Raphson method, which has produced good results in all the range of Weissenberg numbers analyzed ($0 \leq \mathrm{We} \leq 6.5$).

Once the equations have been properly linearized, the advective nature of the constitutive equation, which becomes dominant when the Weissenberg number increases, makes it necessary to use a stabilized finite element formulation to avoid global oscillations. The most widespread method to account for the convective term in the constitutive equation is the so-called SUPG method of Brooks and Hughes [4], first applied to viscoelastic flows by Marchal and Crochet [5]. In a more recent work, Masud et al. [2] use a Variational Multi-Scale (VMS) stabilized method for the momentum–continuity equations and the same SUPG method for the constitutive equation. Other stabilized methods for the viscoelastic fluid problem are the GLS-type methods used for example by Fan et al. [6] and Coronado et al. [7]. Different families of stabilized formulations can also be found in the literature. For example, Li et al. [8] proposed the so-called I–PS–DEVSS–CNBS scheme to stabilize the viscoelastic problem, based on the finite incremental calculus (FIC), pressure stabilization process, the discrete elastic–viscous stress-splitting method (DEVSS), the use of the Crank–Nicolson-based-splitting (CNBS) scheme, and the use of the non-consistent SU method to stabilize the viscoelastic equation. Other two options to circumvent the dominant convective nature of the problem are the fully explicit characteristic based split (CBS) scheme (see [9]) proposed by Nithiarasu [10], with a good performance for a wide range of Weissenberg numbers, and the nonlinear weighted least-squares finite element method proposed by Lee [1]. In the present work, we apply two stabilized formulations based on the VMS framework to control the convective nature of the viscoelastic constitutive equation, different to those just described.

The use of discontinuity-capturing (DC) techniques is not a popular topic in the analysis of viscoelastic flows, but the high elastic stress gradients that appear when the Weissenberg number is increased make it a typical situation where the application of a DC scheme can help. Carew et al. [11] have shown that the inclusion of such a DC technique in a stabilized formulation can improve the stability properties and permits to analyze fluids with a higher elasticity. In the work cited, the numerical diffusion of the discontinuity-capturing term is based on the finite element residual of the constitutive equation, in a similar way to that used by Codina [12] (see also [13]). In the present work we propose a numerical diffusion based on the orthogonal projection of the elastic stress gradient, which represents the *non-captured* part in the finite element approximation.

Referring to the compatibility conditions of inf–sup type for the viscoelastic three-field approximation, they consist of two restrictions on the interpolation spaces, one between pressure and velocity and the other between velocity and the elastic stress (see e.g. [14–16] for background). These two restrictions reduce drastically the choices of stable finite element spaces that allow one to discretize the unknowns. For example, in the paper of Marchal and Crochet [5] one can find different inf–sup stable elements capable to solve the viscoelastic problem. In this classical reference, the authors propose a family of biquadratic velocity and bilinear pressure elements with a multi-bilinear (2×2 or 3×3 or 4×4) stress element for the 2D case. The mathematical analysis of these elements can be found in [17]. It is a clear example of the difficulties to satisfy the two inf–sup conditions associated to the three-field formulation needed in the viscoelastic flow problem. For the tridimensional case, Bogaerds et al. [18] propose a DEVSS-DG stable spatial discretization using tri-quadratic interpolation for velocity, tri-linear interpolation for both pressure and discrete rate of deformation, while the viscoelastic stresses are approximated by discontinuous tri-linear polynomials. In [19] one can find a good review of mixed methods that satisfy the two compatibility conditions required.

The stabilized formulations proposed in this work have their roots in the context of VMS methods introduced by Hughes et al. [20] for the scalar convection–diffusion–reaction problem, and extended later to the vectorial Stokes problem in [21], where the space of the sub-grid scales is taken as orthogonal to the finite element space. As we shall see, this is an important ingredient in the design of our formulations. The purpose of the present paper is precisely to design and test numerically stabilized formulations for the viscoelastic fluid flow problem, permitting the use of equal interpolation between the unknowns (deviatoric elastic stress, velocity and pressure) even in cases where the elastic stress gradients and the elastic component of the fluid are important.

The starting point of a VMS approach is to split the unknowns of the problem into two components, namely, the component that can be approximated by the finite element mesh and the unresolvable one, called sub-grid scale or simply sub-scale in what follows. The latter needs to be approximated in a simple manner in terms of the former, so as to capture its main effect and yield a stable formulation for the finite element unknown. The number of degrees of

freedom is therefore the same as for the Galerkin method. There are different ways to approximate the sub-scale and, in particular, to choose the (finite dimensional) space where it is taken. We will describe two formulations which precisely differ in this choice. Both formulations will allow one to deal with the instabilities of the three-field viscoelastic formulation described earlier. There will be no need to meet the inf–sup conditions for the interpolation spaces and it will be possible to solve convection dominated problems both in the momentum and in the constitutive equation. For the latter, these methods have been found to work well. However, for the momentum equation we have observed that *they are not robust in the presence of high gradients of the unknowns*, and therefore we have had to modify them. The modification consists in designing a sort of *term-by-term stabilization based on the choice of subscales orthogonal to the finite element space*. We will describe in detail this method and the need for it.

The numerical results shown in this work can be separated into three groups. The first (Section 4.1) corresponds to the study of the h-convergence of the formulations proposed for a stationary Oldroyd-B fluid, using linear and quadratic quadrilateral elements. To perform this test we manufacture the solution by introducing a force term computed with a predetermined elastic stress–velocity–pressure solution. The second group (Section 4.2) of results corresponds to the classical 4:1 planar contraction for an Oldroyd-B fluid in the range of Weissenberg numbers $0 \leq \mathrm{We} \leq 5.0$ for a Reynolds number $\mathrm{Re} = 1.0$, and in the range of $0 \leq \mathrm{We} \leq 6.5$ for the quasi non-inertial case $\mathrm{Re} = 0.01$. We compare our results with those published by different authors. The section with numerical examples concludes with a tridimensional example (Section 4.3), only to show that the formulations introduced are immediately extended to the 3D case.

The work is organized as follows. Section 2 contains the presentation of the problem, with the viscoelastic three-field continuous problem, its variational form and the straightforward Galerkin finite element discretization. Section 3 presents our stabilized finite element approach, with the description of the general idea and its application to the present problem. The linearization of the problem and a discontinuity-capturing technique are also discussed. Section 4 contains the numerical results and, finally, in Section 5 conclusions are summarized.

2. The viscoelastic flow problem

2.1. Boundary value problem

Let Ω be the computational domain of $\mathbb{R}^d$ ($d = 2$ or 3) occupied by the fluid, assumed to be bounded and polyhedral, and let $\partial\Omega$ be its boundary. Only stationary problems will be considered in this work. In this case, for incompressible and isothermal viscoelastic flows, the conservation equations for momentum and mass may be expressed as

$$
\begin{aligned}
&-\nabla\cdot\boldsymbol{T} + \rho\boldsymbol{u}\cdot\nabla\boldsymbol{u} + \nabla p = \boldsymbol{f} \quad \text{in } \Omega\\
&\nabla\cdot\boldsymbol{u} = 0 \quad \text{in } \Omega
\end{aligned}
$$

where ρ denotes the constant density, $p : \Omega \longrightarrow \mathbb{R}$ the pressure field, $\boldsymbol{u} : \Omega \longrightarrow \mathbb{R}^d$ the velocity field, $\boldsymbol{f} : \Omega \longrightarrow \mathbb{R}^d$ the force field and $\boldsymbol{T} : \Omega \longrightarrow \mathbb{R}^d \otimes \mathbb{R}^d$ the deviatoric extra stress tensor. In general, $\boldsymbol{T}$ is defined in terms of a viscous and a viscoelastic contribution as

$$\boldsymbol{T} = 2\eta_e\nabla^S\boldsymbol{u} + \boldsymbol{\sigma}$$

where η_e represents the effective viscosity (or solvent viscosity), $\nabla^S\boldsymbol{u}$ is the symmetrical part of the velocity gradient and $\boldsymbol{\sigma}$ is the viscoelastic or elastic stress tensor. For viscoelastic fluids, the problem is incomplete without the definition of a constitutive equation for this viscoelastic stress tensor. A large variety of approaches exist to define it. On the one hand, we have closed integral and differential constitutive models [22] and, on the other, kinetic and molecular dynamics theories [23], that do not yield a closed form constitutive expression. In this work, only the differential Oldroyd-B model is considered. It reads:

$$\boldsymbol{\sigma} + \lambda\overset{\triangledown}{\boldsymbol{\sigma}} - 2\eta_p\nabla^S\boldsymbol{u} = \boldsymbol{0}$$

where λ is the relaxation time, η_p represents the polymeric viscosity and $\overset{\triangledown}{\boldsymbol{\sigma}}$ is the upper convected time derivative of the elastic stress tensor. The sum of the effective and polymeric viscosities gives the total viscosity η_0. We can introduce an additional parameter $\beta \in [0, 1]$ and write η_e and η_p as $\eta_e = \beta\eta_0$ and $\eta_p = (1-\beta)\eta_0$.

The system of equations can be written only in terms of the total viscosity η_0 and β as follows:

$$-\nabla\cdot\boldsymbol{\sigma}-2\beta\eta_0\nabla\cdot\left(\nabla^S\boldsymbol{u}\right)+\rho\boldsymbol{u}\cdot\nabla\boldsymbol{u}+\nabla p=\boldsymbol{f}\quad\text{in }\Omega \tag{1}$$

$$\nabla\cdot\boldsymbol{u}=0\quad\text{in }\Omega \tag{2}$$

$$\frac{1}{2\eta_0}\boldsymbol{\sigma}-(1-\beta)\,\nabla^S\boldsymbol{u}+\frac{\lambda}{2\eta_0}(\boldsymbol{u}\cdot\nabla\boldsymbol{\sigma}-\boldsymbol{\sigma}\cdot\nabla\boldsymbol{u}-(\nabla\boldsymbol{u})^T\cdot\boldsymbol{\sigma})=\boldsymbol{0}\quad\text{in }\Omega \tag{3}$$

where the unknowns are the velocity, the pressure and the viscoelastic stress tensor.

Calling $\boldsymbol{U}=[\boldsymbol{u},p,\boldsymbol{\sigma}]$, $\boldsymbol{F}=[\boldsymbol{f},0,\boldsymbol{0}]$ and defining

$$\mathcal{L}(\hat{\boldsymbol{u}};\boldsymbol{U}):=\begin{pmatrix}-\nabla\cdot\boldsymbol{\sigma}-2\beta\eta_0\nabla\cdot\left(\nabla^S\boldsymbol{u}\right)+\rho\hat{\boldsymbol{u}}\cdot\nabla\boldsymbol{u}+\nabla p\\ \nabla\cdot\boldsymbol{u}\\ \frac{1}{2\eta_0}\boldsymbol{\sigma}-(1-\beta)\,\nabla^S\boldsymbol{u}+\frac{\lambda}{2\eta_0}(\hat{\boldsymbol{u}}\cdot\nabla\boldsymbol{\sigma}-\boldsymbol{\sigma}\cdot\nabla\hat{\boldsymbol{u}}-(\nabla\hat{\boldsymbol{u}})^T\cdot\boldsymbol{\sigma})\end{pmatrix} \tag{4}$$

we may write (1)–(3) as $\mathcal{L}(\boldsymbol{u};\boldsymbol{U})=\boldsymbol{F}$.

Boundary conditions have to be appended to problem (1)–(3). For simplicity in the exposition, we will consider the simplest condition $\boldsymbol{u}=\boldsymbol{0}$ on $\partial\Omega$, and no boundary conditions for $\boldsymbol{\sigma}$. However, in some of the numerical examples we shall specify the viscoelastic stress on inflow boundaries. To avoid this and still get adequate approximations, we would need excessively large computational domains.

For a complete description of the mathematical structure of the problem we refer to [24].

2.2. Variational form

In order to write the weak form of the problem, let us introduce some notation. The space of square integrable functions in a domain ω is denoted by $L^2(\omega)$, and the space of functions whose distributional derivatives of order up to $m\geq 0$ (integer) belong to $L^2(\omega)$ by $H^m(\omega)$. The space $H_0^1(\omega)$ consists of functions in $H^1(\omega)$ vanishing on $\partial\omega$. The topological dual of $H_0^1(\Omega)$ is denoted by $H^{-1}(\Omega)$, the duality pairing being $\langle\cdot,\cdot\rangle$. The L^2 inner product in ω (for scalar, vectors and tensors) is denoted by $(\cdot,\cdot)_\omega$ and the integral over ω of the product of two general functions is written as $\langle\cdot,\cdot\rangle_\omega$, the subscript being omitted when $\omega=\Omega$. The norm in a space X is denoted by $\|\cdot\|_X$, except in the case $X=L^2(\Omega)$, case in which the subscript is omitted.

Using this notation, the stress, velocity and pressure finite element spaces for the continuous problem are $\boldsymbol{\Upsilon}=H^1(\Omega)^{d\times d}_{\text{sym}}$ (symmetric second order tensors with components in $H^1(\Omega)$), $\boldsymbol{V}_0=H_0^1(\Omega)^d$ and $\mathcal{Q}=L^2(\Omega)/\mathbb{R}$, respectively. The weak form of the problem consists in finding $\boldsymbol{U}=[\boldsymbol{u},p,\boldsymbol{\sigma}]\in\boldsymbol{X}:=\boldsymbol{V}_0\times\mathcal{Q}\times\boldsymbol{\Upsilon}$, such that:

$$(\boldsymbol{\sigma},\nabla^S\boldsymbol{v})+2(\beta\eta_0\nabla^S\boldsymbol{u},\nabla^S\boldsymbol{v})+\langle\rho\boldsymbol{u}\cdot\nabla\boldsymbol{u},\boldsymbol{v}\rangle-(p,\nabla\cdot\boldsymbol{v})=\langle\boldsymbol{f},\boldsymbol{v}\rangle$$

$$(q,\nabla\cdot\boldsymbol{u})=0$$

$$\frac{1}{2\eta_0}(\boldsymbol{\sigma},\boldsymbol{\tau})-((1-\beta)\nabla^S\boldsymbol{u},\boldsymbol{\tau})+\frac{\lambda}{2\eta_0}(\boldsymbol{u}\cdot\nabla\boldsymbol{\sigma}-\boldsymbol{\sigma}\cdot\nabla\boldsymbol{u}-(\nabla\boldsymbol{u})^T\cdot\boldsymbol{\sigma},\boldsymbol{\tau})=0$$

for all $\boldsymbol{V}=[\boldsymbol{v},q,\boldsymbol{\tau}]\in\boldsymbol{X}$, where $\boldsymbol{f}\in H^{-1}(\Omega)^d$ is assumed.

In a compact form, the problem can be written as: find $\boldsymbol{U}\in\boldsymbol{X}$ such that

$$B(\boldsymbol{u};\boldsymbol{U},\boldsymbol{V})=\langle\boldsymbol{f},\boldsymbol{v}\rangle \tag{5}$$

for all $\boldsymbol{V}\in\boldsymbol{X}$, where

$$\begin{aligned}B\left(\hat{\boldsymbol{u}};\boldsymbol{U},\boldsymbol{V}\right)=&\,(\boldsymbol{\sigma},\nabla^S\boldsymbol{v})+2(\beta\eta_0\nabla^S\boldsymbol{u},\nabla^S\boldsymbol{v})+\left\langle\rho\hat{\boldsymbol{u}}\cdot\nabla\boldsymbol{u},\boldsymbol{v}\right\rangle-(p,\nabla\cdot\boldsymbol{v})+(q,\nabla\cdot\boldsymbol{u})\\&+\frac{1}{2\eta_0}(\boldsymbol{\sigma},\boldsymbol{\tau})-\left((1-\beta)\,\nabla^S\boldsymbol{u},\boldsymbol{\tau}\right)+\frac{\lambda}{2\eta_0}(\hat{\boldsymbol{u}}\cdot\nabla\boldsymbol{\sigma}-\boldsymbol{\sigma}\cdot\nabla\hat{\boldsymbol{u}}-\left(\nabla\hat{\boldsymbol{u}}\right)^T\cdot\boldsymbol{\sigma},\boldsymbol{\tau}).\end{aligned} \tag{6}$$

2.3. Galerkin finite element discretization

Let $\mathcal{T}_h = \{K\}$ be a finite element partition of the domain Ω. For the sake of conciseness, we consider it quasi-uniform, of diameter h. From this we may construct conforming finite element spaces for the velocity, the pressure and the viscoelastic stress, $\boldsymbol{V}_{h,0} \subset \boldsymbol{V}_0$, $\mathcal{Q}_h \subset \mathcal{Q}$ and $\boldsymbol{\Upsilon}_h \subset \boldsymbol{\Upsilon}$, in the usual manner. The Galerkin finite element approximation consist in finding $\boldsymbol{U}_h = [\boldsymbol{u}_h, p_h, \boldsymbol{\sigma}_h] \in \boldsymbol{X}_h := \boldsymbol{V}_{h,0} \times \mathcal{Q}_h \times \boldsymbol{\Upsilon}_h$ such that:

$$B\left(\boldsymbol{u}_h; \boldsymbol{U}_h, \boldsymbol{V}_h\right) = \langle \boldsymbol{f}, \boldsymbol{v}_h \rangle \tag{7}$$

for all $\boldsymbol{V}_h = [\boldsymbol{v}_h, q_h, \boldsymbol{\tau}_h] \in \boldsymbol{X}_h$.

In principle, we have posed no restrictions on the choice of the finite element spaces. However, there are conditions on these interpolation spaces that must be satisfied in the discrete formulation used. These are the same as for the three-field formulation of the Stokes problem (see for example [25] and references therein), and read as follows: there exist positive constants C_1 and C_2 such that

$$\inf_{q_h \in \mathcal{Q}_h} \sup_{\boldsymbol{v}_h \in \boldsymbol{V}_{h,0}} \frac{(q_h, \nabla \cdot \boldsymbol{v}_h)}{\|q_h\|_{\mathcal{Q}_h} \|\boldsymbol{v}_h\|_{\boldsymbol{V}_{h,0}}} \geq C_1 \tag{8}$$

$$\inf_{\boldsymbol{v}_h \in \boldsymbol{V}_{h,0}} \sup_{\boldsymbol{\tau}_h \in \boldsymbol{\Upsilon}_h} \frac{\left(\boldsymbol{\tau}_h, \nabla^S \boldsymbol{v}_h\right)}{\|\boldsymbol{\tau}_h\|_{\boldsymbol{\Upsilon}_h} \|\boldsymbol{v}_h\|_{\boldsymbol{V}_{h,0}}} \geq C_2. \tag{9}$$

Let us see how to use these conditions for the viscoelastic problem. Using expression (6) and considering that $\boldsymbol{u}_h$ vanishes on $\partial\Omega$, it is readily checked that

$$\begin{aligned} &B(\boldsymbol{u}_h; [\boldsymbol{u}_h, p_h, \boldsymbol{\sigma}_h], [(1-\beta)\boldsymbol{u}_h, (1-\beta)p_h, \boldsymbol{\sigma}_h]) \\ &\quad = 2(1-\beta)\beta\eta_0 \|\nabla^S \boldsymbol{u}_h\|^2 + \frac{1}{2\eta_0}\|\boldsymbol{\sigma}_h\|^2 - \frac{\lambda}{2\eta_0}(\boldsymbol{\sigma}_h \cdot \nabla \boldsymbol{u}_h + (\nabla \boldsymbol{u}_h)^T \cdot \boldsymbol{\sigma}_h, \boldsymbol{\sigma}_h). \end{aligned}$$

Assuming $\lambda \nabla \boldsymbol{u}_h$ to be small enough (in fact, it is only $\lambda \nabla^S \boldsymbol{u}_h$ that needs to be small), this expression provides only control on $\|\boldsymbol{\sigma}_h\|^2$ for all β. One has then to make use of (9) to control $\nabla^S \boldsymbol{u}_h$ and then of (8) to control p_h. It is therefore required that the finite element spaces satisfy (8)–(9) (for more details, see [14,3], for example).

Choosing equal order approximations for $\boldsymbol{\sigma}, \boldsymbol{u}$ and p does not yield a stable scheme. A possible remedy to this situation is to enrich the finite element spaces for the velocity and the stress in order to satisfy both restrictions [5,17]. Another possibility is to use stabilized formulations permitting any interpolation for the variables [8,2,7], which is the approach we pursue in this paper. In general, a stabilized formulation consists of replacing B in (5) by another semilinear form B_h, possibly mesh dependent, with better stability properties.

3. Design of a stable finite element formulation for the viscoelastic flow problem

3.1. Residual based stabilized finite element methods

In the following we present two stabilized finite element formulations for computing viscoelastic flows using the Oldroyd-B constitutive model. They are based on the splitting of the unknowns $\boldsymbol{U}$ in a component $\boldsymbol{U}_h$ which can be resolved by the finite element space, and the remainder $\tilde{\boldsymbol{U}}$, that will be called sub-grid scale. The framework we use is based on [20].

We will omit the details of the derivation of the method. In the context of a three-field formulation for flow problems, they can be found in [26]. Here we just state the method for the particular case of stationary viscoelastic flows. After some approximations, this method consists in finding $\boldsymbol{U}_h \in \boldsymbol{X}_h$ such that

$$B(\boldsymbol{u}; \boldsymbol{U}_h, \boldsymbol{V}_h) + \sum_K \langle \tilde{\boldsymbol{U}}, \mathcal{L}^*(\boldsymbol{u}_h; \boldsymbol{V}_h) \rangle_K = \langle \boldsymbol{f}, \boldsymbol{v}_h \rangle \tag{10}$$

for all $\boldsymbol{V}_h \in \boldsymbol{X}_h$, where $\mathcal{L}^*(\hat{\boldsymbol{u}}; \boldsymbol{V})$ is the formal adjoint of the operator in (4) without considering boundary conditions, which is given by

$$\mathcal{L}^*(\hat{\boldsymbol{u}};\boldsymbol{V}) := \begin{pmatrix} (1-\beta)\nabla\cdot\boldsymbol{\tau} - 2\beta\eta_0\nabla\cdot\left(\nabla^S\boldsymbol{v}\right) - \rho\hat{\boldsymbol{u}}\cdot\nabla\boldsymbol{v} - \nabla q \\ -\nabla\cdot\boldsymbol{v} \\ \dfrac{1}{2\eta_0}\boldsymbol{\tau} + \nabla^S\boldsymbol{v} + \dfrac{\lambda}{2\eta_0}\left(-\hat{\boldsymbol{u}}\cdot\nabla\boldsymbol{\tau} - \boldsymbol{\tau}\cdot(\nabla\hat{\boldsymbol{u}})^T - \nabla\hat{\boldsymbol{u}}\cdot\boldsymbol{\tau}\right) \end{pmatrix}$$

and $\tilde{\boldsymbol{U}}$ is the sub-grid scale, which needs to be approximated. If $\tilde{P}$ is the L^2 projection onto the space of sub-grid scales, the approximation we consider within each element is

$$\tilde{\boldsymbol{U}} = \boldsymbol{\alpha}\tilde{P}[\boldsymbol{F} - \mathcal{L}(\boldsymbol{u}_h;\boldsymbol{U}_h)] \tag{11}$$

where $\boldsymbol{\alpha}$ is a matrix computed within each element, which we take as

$$\boldsymbol{\alpha} = \mathrm{diag}(\alpha_1\boldsymbol{I}_d, \alpha_2, \alpha_3\boldsymbol{I}_{d\times d}) \tag{12}$$

with $\boldsymbol{I}_d$ the identity on vectors of $\mathbb{R}^d$, $\boldsymbol{I}_{d\times d}$ the identity on second order tensors and the parameters $\alpha_i,\ i=1,2,3$, are computed as (see [25,26])

$$\alpha_1 = \left[c_1\frac{\eta_0}{h_1^2} + c_2\frac{\rho\,|\boldsymbol{u}_h|}{h_2}\right]^{-1}$$
$$\alpha_2 = \frac{h_1^2}{c_1\alpha_1}$$
$$\alpha_3 = \left[c_3\frac{1}{2\eta_0} + c_4\left(\frac{\lambda}{2\eta_0}\frac{|\boldsymbol{u}_h|}{h_2} + \frac{\lambda}{\eta_0}|\nabla\boldsymbol{u}_h|\right)\right]^{-1}.$$

In these expressions, h_1 corresponds to a characteristic length calculated as the square root of the element area in the 2D case and the cubic root of the element volume in 3D, and h_2 corresponds to another characteristic length calculated as the element length in the streamline direction. The term $|\boldsymbol{u}_h|$ is the Euclidean norm of the velocity, and $|\nabla\boldsymbol{u}_h|$ the Frobenius norm of the velocity gradient (another possibility for this last term is to take the maximum eigenvalue of the velocity gradient matrix). The constants $c_i,\ i=1,4$ are algorithmic parameters in the formulation. The values used in this work for linear elements are $c_1 = 4.0,\ c_2 = 2.0,\ c_3 = 4.0$ and $c_4 = 0.25$. For higher order elements, the characteristic lengths h_1 and h_2 are respectively divided by k^2 and k, k being the order of the finite element interpolation, and we keep the value of the constants used for linear elements.

Inserting (11) with $\boldsymbol{\alpha}$ given in (12) in (10) we get the following method: find $\boldsymbol{U}_h \in \boldsymbol{X}_h$ such that

$$B(\boldsymbol{u}_h;\boldsymbol{U}_h,\boldsymbol{V}_h) + S_1(\boldsymbol{u}_h;\boldsymbol{U}_h,\boldsymbol{V}_h) + S_2(\boldsymbol{U}_h,\boldsymbol{V}_h) + S_3(\boldsymbol{u}_h;\boldsymbol{U}_h,\boldsymbol{V}_h) = \langle\boldsymbol{f},\boldsymbol{v}_h\rangle + R_1(\boldsymbol{u}_h;\boldsymbol{V}_h) \tag{13}$$

for all $\boldsymbol{V}_h \in \boldsymbol{X}_h$, where

$$\begin{aligned} S_1(\hat{\boldsymbol{u}}_h;\boldsymbol{U}_h,\boldsymbol{V}_h) \;=\; & \sum_K \alpha_1\Big\langle\tilde{P}\Big[-\nabla\cdot\boldsymbol{\sigma}_h - 2\beta\eta_0\nabla\cdot\left(\nabla^S\boldsymbol{u}_h\right) + \rho\hat{\boldsymbol{u}}_h\cdot\nabla\boldsymbol{u}_h + \nabla p_h\Big], \\ & -(1-\beta)\nabla\cdot\boldsymbol{\tau}_h + 2\beta\eta_0\nabla\cdot\left(\nabla^S\boldsymbol{v}_h\right) + \rho\hat{\boldsymbol{u}}_h\cdot\nabla\boldsymbol{v}_h + \nabla q_h\Big\rangle_K \end{aligned} \tag{14}$$

$$S_2(\boldsymbol{U}_h,\boldsymbol{V}_h) = \sum_K \alpha_2\Big\langle\tilde{P}[\nabla\cdot\boldsymbol{v}_h], \nabla\cdot\boldsymbol{u}_h\Big\rangle_K \tag{15}$$

$$\begin{aligned} S_3(\hat{\boldsymbol{u}}_h;\boldsymbol{U}_h,\boldsymbol{V}_h) \;=\; & \sum_K \alpha_3\Big\langle\tilde{P}\Big[\frac{1}{2\eta_0}\boldsymbol{\sigma}_h - (1-\beta)\nabla^S\boldsymbol{u}_h + \frac{\lambda}{2\eta_0}\left(\hat{\boldsymbol{u}}_h\cdot\nabla\boldsymbol{\sigma}_h - \boldsymbol{\sigma}_h\cdot\nabla\hat{\boldsymbol{u}}_h - (\nabla\hat{\boldsymbol{u}}_h)^T\cdot\boldsymbol{\sigma}_h\right)\Big], \\ & -\frac{1}{2\eta_0}\boldsymbol{\tau}_h - \nabla^S\boldsymbol{v}_h + \frac{\lambda}{2\eta_0}\left(\hat{\boldsymbol{u}}_h\cdot\nabla\boldsymbol{\tau}_h + \boldsymbol{\tau}_h\cdot(\nabla\hat{\boldsymbol{u}}_h)^T + \nabla\hat{\boldsymbol{u}}_h\cdot\boldsymbol{\tau}_h\right)\Big\rangle_K \end{aligned} \tag{16}$$

$$R_1(\hat{\boldsymbol{u}}_h;\boldsymbol{V}_h) = \sum_K \alpha_1\Big\langle\tilde{P}[\boldsymbol{f}], -(1-\beta)\nabla\cdot\boldsymbol{\tau}_h + 2\beta\eta_0\nabla\cdot\left(\nabla^S\boldsymbol{v}_h\right) + \rho\hat{\boldsymbol{u}}_h\cdot\nabla\boldsymbol{v}_h + \nabla q_h\Big\rangle_K. \tag{17}$$

In these equations, $\tilde{P}$ is the projection restricted to the appropriate space of the components of the finite element residual $\boldsymbol{R}_h := \boldsymbol{F} - \mathcal{L}(\boldsymbol{u}_h; \boldsymbol{U}_h)$. It remains only to define this projection, for which we consider two possible choices as in [26]:

- Algebraic sub-grid scale (ASGS) method: $\tilde{P} = I$ (the identity) when applied to finite element residuals.
- Orthogonal sub-grid scale (OSGS) method: $\tilde{P} = P_h^{\perp} = I - P_h$, where P_h is the L^2 projection onto the appropriate finite element space.

For the analysis of the ASGS and the OSGS methods for the linearized Navier–Stokes equations using the classical velocity–pressure formulation, see [27,28], respectively.

Independently of the choice of the projection $\tilde{P}$, method (13) is consistent, since the terms added to the Galerkin ones are proportional to the finite element residual $\boldsymbol{R}_h$. Thus, they vanish if the finite element solution is replaced by the solution of the continuous problem $\boldsymbol{U}$. It is in this sense that we call (13) a *residual based* method.

3.2. Split OSGS stabilization

For smooth solutions, method (13) is stable and displays optimal order of convergence, both for $\tilde{P} = I$ and for $\tilde{P} = P_h^{\perp}$. In our experience for Newtonian flows, the OSGS method is in general more accurate, whereas the ASGS is cheaper, since projections are not needed, and sometimes more robust. Note that the OSGS will be, by construction, less dissipative.

If we consider the case $\tilde{P} = P_h^{\perp}$, from (13) we can design *a simplified method*, which consists in *neglecting the cross local inner-product terms* in (13), as well as some other terms that do not contribute to stability. In particular, the term $S_1(\hat{\boldsymbol{u}}_h; \boldsymbol{U}_h, \boldsymbol{V}_h)$ in (14) can in principle be replaced by

$$(1-\beta)\sum_K \alpha_1 \left\langle P_h^{\perp}\left[\nabla\cdot\boldsymbol{\sigma}_h\right], \nabla\cdot\boldsymbol{\tau}_h\right\rangle_K - \beta^2 \sum_K \alpha_1 \left\langle P_h^{\perp}\left[2\eta_0 \nabla\cdot(\nabla^S \boldsymbol{u}_h)\right], 2\eta_0 \nabla\cdot(\nabla^S \boldsymbol{v}_h)\right\rangle_K$$
$$+ \sum_K \alpha_1 \left\langle P_h^{\perp}\left[\rho\hat{\boldsymbol{u}}_h\cdot\nabla\boldsymbol{u}_h\right], \rho\hat{\boldsymbol{u}}_h\cdot\nabla\boldsymbol{v}_h\right\rangle_K + \sum_K \alpha_1 \left\langle P_h^{\perp}\left[\nabla p_h\right], \nabla q_h\right\rangle_K \tag{18}$$

and, since the second term does not contribute to stability, it can be also deleted, like the term $R_1(\boldsymbol{u}_h; \boldsymbol{V}_h)$ on the right-hand-side of (13). The three remaining terms in (18) help to improve stability, the first giving control on the divergence of the viscoelastic stress, the third on the convective term and the fourth on the pressure gradient. This term-by-term stabilization point of view is in fact previous to the OSGS method, based on the approximation of the sub-grid scales. It is proposed in [21] and analyzed in [28].

The key point that allows one to add (18) to the Galerkin terms is the orthogonal projection $P_h^{\perp}$. Obviously, (18) is not zero when the finite element solution is replaced by the continuous solution, and therefore the method is not consistent in the sense used in the finite element context. However, *the consistency error is of optimal order*, since for any smooth enough function f, $P_h(f)$ is an optimal approximation to f in the finite element space, and therefore $P_h^{\perp}(f)$ goes to zero with h at the optimal rate permitted by the finite element interpolation (and the smoothness of f).

The method in (13) is consistent for any projection $\tilde{P}$, and therefore there we might consider $\tilde{P} = I - P_{h,0}$ for the projection applied to the residual of the momentum equation, where $P_{h,0}$ is the L^2 projection onto the velocity finite element space *incorporating* boundary conditions, i.e., the L^2 projection onto $\boldsymbol{V}_{h,0}$. However, in (18) we need to take $P_h^{\perp} = I - P_h$, P_h being the L^2 projection *without* boundary conditions, since otherwise $P_h^{\perp}(f)$ would not converge to zero at the optimal order mentioned before. The price to be paid is that the finite element mesh needs to satisfy a mild compatibility condition, as explained in [28], which is easily fulfilled for most meshes.

Apart from $P_h^{\perp}$, other projections can be used in (18), as soon as one can guarantee that they provide enough stability and that the consistency error introduced has optimal order. Among these, let us mention those associated to the Local Projection Stabilization (see for example [29,30] and references therein) or the method proposed in [31] for the Stokes problem. These local projections avoid the global projection P_h that we have used, which requires to solve a linear system (trivial to solve, though). This might seem an advantage of local projections. However, the bottleneck of these methods is that they all increase the sparsity of the final matrix. This is usually unaffordable, and therefore

an iterative strategy is needed anyway. In our case, we solve the problem by lagging the projection one iteration in the iterative process, as described below. This is for free in nonlinear problems as the one considered in this paper. Furthermore, it is shown in [28] that the Galerkin method already gives control on the finite element component of the different terms of the equation, and therefore only control on the component orthogonal to the finite element space is required. Thus, *any* projection different to the L^2 one will introduce more numerical dissipation for the same stability.

Similar considerations can be applied to modify the term $S_3(\hat{\boldsymbol{u}}_h; \boldsymbol{U}_h, \boldsymbol{V}_h)$ in (16), now taking into account that $P_h^{\perp}(\boldsymbol{\sigma}_h) = \boldsymbol{0}$ ($P_h^{\perp}$ being now the orthogonal projection to the space of viscoelastic stresses). Therefore, the modified method we propose, that we call the *split OSGS method*, is: find $\boldsymbol{U}_h \in \boldsymbol{X}_h$ such that

$$B(\boldsymbol{u}_h; \boldsymbol{U}_h, \boldsymbol{V}_h) + S_1^{\perp}(\boldsymbol{u}_h; \boldsymbol{U}_h, \boldsymbol{V}_h) + S_2^{\perp}(\boldsymbol{U}_h, \boldsymbol{V}_h) + S_3^{\perp}(\boldsymbol{u}_h; \boldsymbol{U}_h, \boldsymbol{V}_h) = \langle \boldsymbol{f}, \boldsymbol{v}_h \rangle \tag{19}$$

for all $\boldsymbol{V}_h \in \boldsymbol{X}_h$, where

$$\begin{aligned} S_1^{\perp}(\hat{\boldsymbol{u}}_h; \boldsymbol{U}_h, \boldsymbol{V}_h) \;=\; & (1-\beta) \sum_K \alpha_1 \Big\langle P_h^{\perp}\big[\nabla \cdot \boldsymbol{\sigma}_h\big], \nabla \cdot \boldsymbol{\tau}_h \Big\rangle_K \\ & + \sum_K \alpha_1 \Big\langle P_h^{\perp}\big[\rho \hat{\boldsymbol{u}}_h \cdot \nabla \boldsymbol{u}_h\big], \rho \hat{\boldsymbol{u}}_h \cdot \nabla \boldsymbol{v}_h \Big\rangle_K + \sum_K \alpha_1 \Big\langle P_h^{\perp}\big[\nabla p_h\big], \nabla q_h \Big\rangle_K \end{aligned} \tag{20}$$

$$S_2^{\perp}(\boldsymbol{U}_h, \boldsymbol{V}_h) = \sum_K \alpha_2 \Big\langle P_h^{\perp}[\nabla \cdot \boldsymbol{u}_h], \nabla \cdot \boldsymbol{v}_h \Big\rangle_K \tag{21}$$

$$\begin{aligned} S_3^{\perp}(\hat{\boldsymbol{u}}_h; \boldsymbol{U}_h, \boldsymbol{V}_h) \;=\; & (1-\beta) \sum_K \alpha_3 \Big\langle P_h^{\perp}\big[\nabla^S \boldsymbol{u}_h\big], \nabla^S \boldsymbol{v}_h \Big\rangle_K + \frac{\lambda^2}{4\eta_0^2} \sum_K \alpha_3 \Big\langle P_h^{\perp}\big[\hat{\boldsymbol{u}}_h \cdot \nabla \boldsymbol{\sigma}_h\big], \hat{\boldsymbol{u}}_h \cdot \nabla \boldsymbol{\tau}_h \Big\rangle_K \\ & - \frac{\lambda^2}{4\eta_0^2} \sum_K \alpha_3 \Big\langle P_h^{\perp}\big[\boldsymbol{\sigma}_h \cdot \nabla \hat{\boldsymbol{u}}_h + (\nabla \hat{\boldsymbol{u}}_h)^T \cdot \boldsymbol{\sigma}_h\big], \boldsymbol{\tau}_h \cdot (\nabla \hat{\boldsymbol{u}}_h)^T + \nabla \hat{\boldsymbol{u}}_h \cdot \boldsymbol{\tau}_h \Big\rangle_K . \end{aligned} \tag{22}$$

The stabilizing mechanism introduced by the different terms in these expressions is clear. The term $S_1^{\perp}$ has already been discussed. Regarding the term $S_3^{\perp}$ in (22) it is observed that the first part has an EVSS-like structure (see [32]), that now has been derived from a simplification of the OSGS method, whereas the second part has a streamline-upwind structure, but the introduction of the orthogonal projection $P_h^{\perp}$ makes it have an optimal consistency error.

The method (19) is not just a simplification of (13). *For smooth solutions*, both have an optimal convergence rate in h. However, *in problems where the solution has strong gradients*, we have found (19) more robust. The split form of the OSGS formulation in the continuity and in the momentum equation has been applied and chosen after a large number of numerical tests. This method shows better response than the non-split formulation in the solution of pressure and stress, and gives the possibility to resolve problems where the elastic component is higher. When using (14), the terms that we have identified as "problematic" are the cross-terms $\alpha_1 \langle \nabla p_h, -(1-\beta)\nabla \cdot \boldsymbol{\tau}_h \rangle_K$ and $\alpha_1 \langle -\nabla \cdot \boldsymbol{\sigma}_h, \nabla q_h \rangle_K$. In the presence of high derivatives of pressure and stresses, such as in the corner of the 4:1 contraction example in Section 4.2, they lead to convergence difficulties for high Weissenberg numbers and to inaccurate localization of pressure and stress peaks.

We have not observed important differences in the use of either $S_3(\hat{\boldsymbol{u}}_h; \boldsymbol{U}_h, \boldsymbol{V}_h)$ in (16) or the modification $S_3^{\perp}(\hat{\boldsymbol{u}}_h; \boldsymbol{U}_h, \boldsymbol{V}_h)$ in (22). The former allows us to consider $\tilde{P} = I$ or $\tilde{P} = P_h^{\perp}$, and this is what we will compare in the numerical examples. So, in these examples we will use the terminology S-ASGS when (16) is used with $\tilde{P} = I$ and S-OSGS when (16) is used with $\tilde{P} = P_h^{\perp}$, but in both cases we will use (20) and (21) instead of (14) and (15).

3.3. Discontinuity capturing technique

The stabilized finite element formulation presented above yields a *globally* stable solution, i.e., norms of the unknowns over the whole domain Ω are bounded. However, if the solution displays very high gradients, local oscillations may still remain. In order to avoid this, or at least to alleviate this problem, we have introduced a discontinuity-capturing (DC) or shock-capturing term in our numerical formulation. In general, the main idea of any DC technique is to increase the amount of numerical dissipation in the neighborhood of layers (see [12], for example).

In viscoelastic flow problems, we can find local instabilities or very high gradients in the pressure and in the viscoelastic stress components when the fluid flow finds an abrupt change in the geometry. This gradient can be especially strong when the amount of elastic component in the fluid is important.

The constitutive equation is of convective–reactive nature. The advection velocity is $\boldsymbol{u}_h$ (in the discrete problem) and the reactive terms are proportional to the velocity gradient $\nabla \boldsymbol{u}_h$. Therefore, if a non-consistent artificial diffusion is to be introduced, it must be of the form

$$k_\sigma = C_a h_1 \left|\boldsymbol{u}_h\right| + C_b \left|\nabla \boldsymbol{u}_h\right| h_1^2. \tag{23}$$

The characteristic lengths give dimensional consistency, and the parameters C_a and C_b are algorithmic constants.

If an artificial diffusion term is added to problem (19), with the diffusion given by (23), the consistency error would make the method converge at most with an order $\mathcal{O}(h^{1/2})$. In order to design a method that can yield optimal convergence, at least when the solution is smooth, a possible option is to multiply the diffusion in (23) by a term proportional to the residual of the equation being solved properly normalized (see [12] and references therein). In this case, the residual would be that of the constitutive equation, as in [11]. However, in this work we have used another switch to activate the numerical diffusion, which is to make it proportional to the component of the viscoelastic stress orthogonal to the finite element space, that is to say, we take as diffusion coefficient

$$k_\sigma = \left(C_a h \left|\boldsymbol{u}_h\right| + C_b \left|\nabla \boldsymbol{u}_h\right| h^2\right) \frac{\left|P_h^\perp \left(\nabla \boldsymbol{\sigma}_h\right)\right|}{\left|\nabla \boldsymbol{\sigma}_h\right|} \tag{24}$$

instead of (23). The way to introduce the DC dissipation is to add the term

$$\sum_K k_\sigma \left\langle \nabla \boldsymbol{\sigma}_h, \nabla \boldsymbol{\tau}_h \right\rangle_K$$

to the left-hand-side of (19), where $\boldsymbol{\tau}_h$ is the test function of the constitutive equation.

The values used in this work for the constants appearing in the numerical diffusion are $C_a = 0.1$ and $C_b = 0.5$.

3.4. Linearized problem

The equations for incompressible viscoelastic flows have several non-linear terms, both in the momentum and in the constitutive equations. In the former we have the convective term, and in the latter we have the term corresponding to convection of stresses and the rotational terms arising from the objective derivative of stresses. On top of that, the stabilization terms depend also on the velocity, introducing therefore additional nonlinearities.

As it is usual for incompressible flow problems, for the convective term of the momentum equation we can use a fixed point scheme, taking the advection velocity of the previous iteration. This leads only to first order convergence, but it is a robust option. However, for the nonlinear terms in the constitutive equation we have found crucial to use a Newton–Raphson linearization. This has allowed us to reach higher Weissenberg numbers.

The equations to be solved at each iteration are written in Algorithm 1. To understand them, let us make the following remarks:

- The nonlinear term in the momentum equation can be linearized with the fixed point scheme or with Newton–Raphson's method. This corresponds respectively to $N_u = 0$ and $N_u = 1$. Newton's iterations are only considered for the Galerkin contribution in the constitutive equation.
- Only a fixed point scheme is considered for the stabilization terms of the constitutive equation.
- The stabilization parameters are computed with values of the unknowns at the previous iterations. This is why a superscript $i - 1$ has been used for them.
- The orthogonal projection of any function f has been approximated as $P_h^\perp(f^i) \approx f^i - P_h(f^{i-1})$. The iterative treatment of the orthogonal projection is thus coupled to the linearization of the whole system.
- The ASGS method for the constitutive equation corresponds to $\tilde{P} = I$, whereas the OSS method corresponds to $\tilde{P} = P_h^\perp$. In this case, the same strategy as for the rest of orthogonal projections is used.
- The DC dissipation is linearized using a fixed point strategy.

Algorithm 1 Fully discrete and linearized problem at each iteration

Given $\boldsymbol{u}_h^{i-1}$, $\boldsymbol{\sigma}_h^{i-1}$ ($i \geq 1$), solve for $\boldsymbol{u}_h^i$, p_h^i, $\boldsymbol{\sigma}_h^i$ from:

$$
\begin{aligned}
&(\boldsymbol{\sigma}_h^i, \nabla^S \boldsymbol{v}_h) + 2(\beta\eta_0 \nabla^S \boldsymbol{u}_h^i, \nabla^S \boldsymbol{v}_h) + \left\langle \rho \boldsymbol{u}_h^{i-1} \cdot \nabla \boldsymbol{u}_h^i, \boldsymbol{v}_h \right\rangle + N_u \left\langle \rho \boldsymbol{u}_h^i \cdot \nabla \boldsymbol{u}_h^{i-1}, \boldsymbol{v}_h \right\rangle \\
&\quad - (p_h^i, \nabla \cdot \boldsymbol{v}_h) + (q_h, \nabla \cdot \boldsymbol{u}_h^i) + \frac{1}{2\eta_0}(\boldsymbol{\sigma}_h^i, \boldsymbol{\tau}_h) - ((1-\beta)\nabla^S \boldsymbol{u}_h^i, \boldsymbol{\tau}_h) \\
&\quad + \frac{\lambda}{2\eta_0}(\boldsymbol{u}_h^{i-1} \cdot \nabla \boldsymbol{\sigma}_h^i - \boldsymbol{\sigma}_h^i \cdot \nabla \boldsymbol{u}_h^{i-1} - (\nabla \boldsymbol{u}_h^{i-1})^T \cdot \boldsymbol{\sigma}_h^i, \boldsymbol{\tau}_h) \\
&\quad + \frac{\lambda}{2\eta_0}(\boldsymbol{u}_h^i \cdot \nabla \boldsymbol{\sigma}_h^{i-1} - \boldsymbol{\sigma}_h^{i-1} \cdot \nabla \boldsymbol{u}_h^i - (\nabla \boldsymbol{u}_h^i)^T \cdot \boldsymbol{\sigma}_h^{i-1}, \boldsymbol{\tau}_h) \\
&\quad + (1-\beta) \sum_K \alpha_1^{i-1} \left\langle \nabla \cdot \boldsymbol{\sigma}_h^i, \nabla \cdot \boldsymbol{\tau}_h \right\rangle_K \\
&\quad + \sum_K \alpha_1^{i-1} \left\langle \rho \boldsymbol{u}_h^{i-1} \cdot \nabla \boldsymbol{u}_h^i, \rho \boldsymbol{u}_h^{i-1} \cdot \nabla \boldsymbol{v}_h \right\rangle_K + \sum_K \alpha_1^{i-1} \left\langle \nabla p_h^i, \nabla q_h \right\rangle_K \\
&\quad + \sum_K \alpha_2^{i-1} \left\langle \nabla \cdot \boldsymbol{u}_h^i, \nabla \cdot \boldsymbol{v}_h \right\rangle_K \\
&\quad + \sum_K \alpha_3^{i-1} \Big\langle \tilde{P}\Big[\frac{1}{2\eta_0} \boldsymbol{\sigma}_h^i - (1-\beta)\nabla^S \boldsymbol{u}_h^i + \frac{\lambda}{2\eta_0} \Big(\boldsymbol{u}_h^{i-1} \cdot \nabla \boldsymbol{\sigma}_h^i - \boldsymbol{\sigma}_h^i \cdot \nabla \boldsymbol{u}_h^{i-1} - (\nabla \boldsymbol{u}_h^{i-1})^T \cdot \boldsymbol{\sigma}_h^i \Big) \Big], \\
&\qquad\quad - \frac{1}{2\eta_0} \boldsymbol{\tau}_h - \nabla^S \boldsymbol{v}_h + \frac{\lambda}{2\eta_0} \Big(\boldsymbol{u}_h^{i-1} \cdot \nabla \boldsymbol{\tau}_h + \boldsymbol{\tau}_h \cdot (\nabla \boldsymbol{u}_h^{i-1})^T + \nabla \boldsymbol{u}_h^{i-1} \cdot \boldsymbol{\tau}_h \Big) \Big\rangle_K \\
&\quad + \sum_K k_\sigma^{i-1} \left\langle \nabla \boldsymbol{\sigma}_h^i, \nabla \boldsymbol{\tau}_h \right\rangle_K \\
&= \langle \boldsymbol{f}, \boldsymbol{v}_h \rangle + \left\langle 2\beta\eta_0 \nabla \cdot (\nabla^S \boldsymbol{v}_h) + \rho \boldsymbol{u}_h^{i-1} \cdot \nabla \boldsymbol{v}_h + \nabla q_h \right\rangle_K \\
&\quad + N_u \left\langle \rho \boldsymbol{u}_h^{i-1} \cdot \nabla \boldsymbol{u}_h^{i-1}, \boldsymbol{v}_h \right\rangle \\
&\quad + \frac{\lambda}{2\eta_0}(\boldsymbol{u}_h^{i-1} \cdot \nabla \boldsymbol{\sigma}_h^{i-1} - \boldsymbol{\sigma}_h^{i-1} \cdot \nabla \boldsymbol{u}_h^{i-1} - (\nabla \boldsymbol{u}_h^{i-1})^T \cdot \boldsymbol{\sigma}_h^{i-1}, \boldsymbol{\tau}_h) \\
&\quad + (1-\beta) \sum_K \alpha_1^{i-1} \left\langle P_h[\nabla \cdot \boldsymbol{\sigma}_h^{i-1}], \nabla \cdot \boldsymbol{\tau}_h \right\rangle_K \\
&\quad + \sum_K \alpha_1^{i-1} \left\langle P_h[\rho \boldsymbol{u}_h^{i-1} \cdot \nabla \boldsymbol{u}_h^{i-1}], \rho \boldsymbol{u}_h^{i-1} \cdot \nabla \boldsymbol{v}_h \right\rangle_K + \sum_K \alpha_1^{i-1} \left\langle P_h[\nabla p_h^{i-1}], \nabla q_h \right\rangle_K \\
&\quad + \sum_K \alpha_2^{i-1} \left\langle P_h[\nabla \cdot \boldsymbol{u}_h^{i-1}], \nabla \cdot \boldsymbol{v}_h \right\rangle_K
\end{aligned}
$$

for all test functions $\boldsymbol{v}_h$, $\boldsymbol{\tau}_h$ and q_h.

The equations in Algorithm 1 need to be embedded in a general algorithm which defines the nonlinear strategy to be used. In this respect, apart from the linearization of the different terms just described, we have found useful to use two more numerical ingredients, namely, an under-relaxation scheme and a continuation method in terms of the relaxation time λ. Concerning the former, we always use a relaxation parameter $\varepsilon = 0.5$, which we have found useful to set by default (even when it might not be necessary). Referring to the continuation method, we use when needed a simple continuation technique, consisting in N_λ continuation steps of equal size $\delta\lambda = \lambda/N_\lambda$. Moreover, we couple the continuation loop with the linearization loop, although both loops could also be treated in a nested way.

With these comments in mind, the final algorithm is presented in Algorithm 2.

Algorithm 2 General algorithm

SET $\boldsymbol{u}_h^0 = \boldsymbol{0}$, $\boldsymbol{\sigma}_h^0 = \boldsymbol{0}$, $p_h^0 = 0$
SET $\lambda^0 = 0$, $k_\sigma^0 = 0$
  SET $i = 0$
  WHILE not converged DO:
    $i \leftarrow i + 1$
    SET the relaxation time to $\lambda^i = \max(\lambda^{i-1} + \lambda/N_\lambda, \lambda)$
    COMPUTE projections $P_h\left(\rho \boldsymbol{u}_h^{i-1} \cdot \nabla \boldsymbol{u}_h^{i-1}\right)$, $P_h\left(\nabla \cdot \boldsymbol{\sigma}_h^{i-1}\right)$, $P_h\left(\nabla p_h^{i-1}\right)$, $P_h\left(\nabla \cdot \boldsymbol{u}_h^{i-1}\right)$
    COMPUTE the stabilization parameters α_1^{i-1}, α_2^{i-1}, α_3^{i-1}
    COMPUTE k_σ^{i-1} from (23), if needed.
    SOLVE the equations in Algorithm 1
    UPDATE unknowns:
      $\boldsymbol{u}_h^i \leftarrow \varepsilon \boldsymbol{u}_h^i + (1-\varepsilon)\, \boldsymbol{u}_h^{i-1}$
      $p_h^i \leftarrow \varepsilon p_h^i + (1-\varepsilon)\, p_h^{i-1}$
      $\boldsymbol{\sigma}_h^i \leftarrow \varepsilon \boldsymbol{\sigma}_h^i + (1-\varepsilon)\, \boldsymbol{\sigma}_h^{i-1}$
    CHECK convergence
  END WHILE

4. Numerical results

In this section, some tests are conducted to show the numerical performance of the proposed stabilized formulations and the benefits of the inclusion of a DC technique in the constitutive equation for the viscoelastic stress.

The first example is a convergence test with a manufactured solution. It serves to show that in the case of smooth solutions the formulations presented are optimally convergent. In fact, in this case also the original residual-based formulations yield optimal convergence. However, these formulations perform poorly in the example of Section 4.2, where the classical 4:1 flow contraction problem is solved. Peaks of stresses and pressure at the corner are not properly captured, and this is precisely the reason that has led us to the split OSGS formulation. This section concludes with a tridimensional extension of the contraction problem in Section 4.3.

4.1. Convergence test

The first set of results shown corresponds to the convergence study of the stabilized formulations presented for the viscoelastic fluid problem. A force term is introduced both in the momentum and constitutive equations so that the exact solution is given by:

$$
\begin{aligned}
u_x(x, y) &= 2x^2 y\,(x-1)^2\,(y-1)^2\,(2y-1)\\
u_y(x, y) &= 2xy^2\,(x-1)^2\,(y-1)^2\,(2x-1)\\
p(x, y) &= \sin(2\pi x)\sin(2\pi y)\\
\sigma_{xx}(x, y) &= 5\sin(2\pi x)\sin(2\pi y)\\
\sigma_{yy}(x, y) &= -5\sin(2\pi x)\sin(2\pi y)\\
\sigma_{xy}(x, y) &= \sin(2\pi x)\sin(2\pi y)
\end{aligned}
$$

where the x and y components of the velocity and the stress have been indicated with a subscript.

Of course these velocity and stress fields do not satisfy the constitutive equation (3), with a zero right-hand-side. We have added a forcing term in this equation given by

$$
\boldsymbol{f_C} = \frac{1}{2\eta_0}\boldsymbol{\sigma} - (1-\beta)\,\nabla^S \boldsymbol{u} + \frac{\lambda}{2\eta_0}\left(\boldsymbol{u}\cdot\nabla\boldsymbol{\sigma} - \boldsymbol{\sigma}\cdot\nabla\boldsymbol{u} - (\nabla\boldsymbol{u})^T\cdot\boldsymbol{\sigma}\right) \quad \text{in } \Omega
$$

with $\boldsymbol{u}$ and $\boldsymbol{\sigma}$ the manufactured solution given above.

The computational domain is the unit square, discretized using uniform structured meshes of bilinear and biquadratic quadrilateral elements, the range of element sizes being $0.0030625 < h < 0.0125$ in the bilinear case (Fig. 1, left), and $0.005 < h < 0.025$ in the biquadratic case (see Fig. 1, right). For each mesh, we have solved the

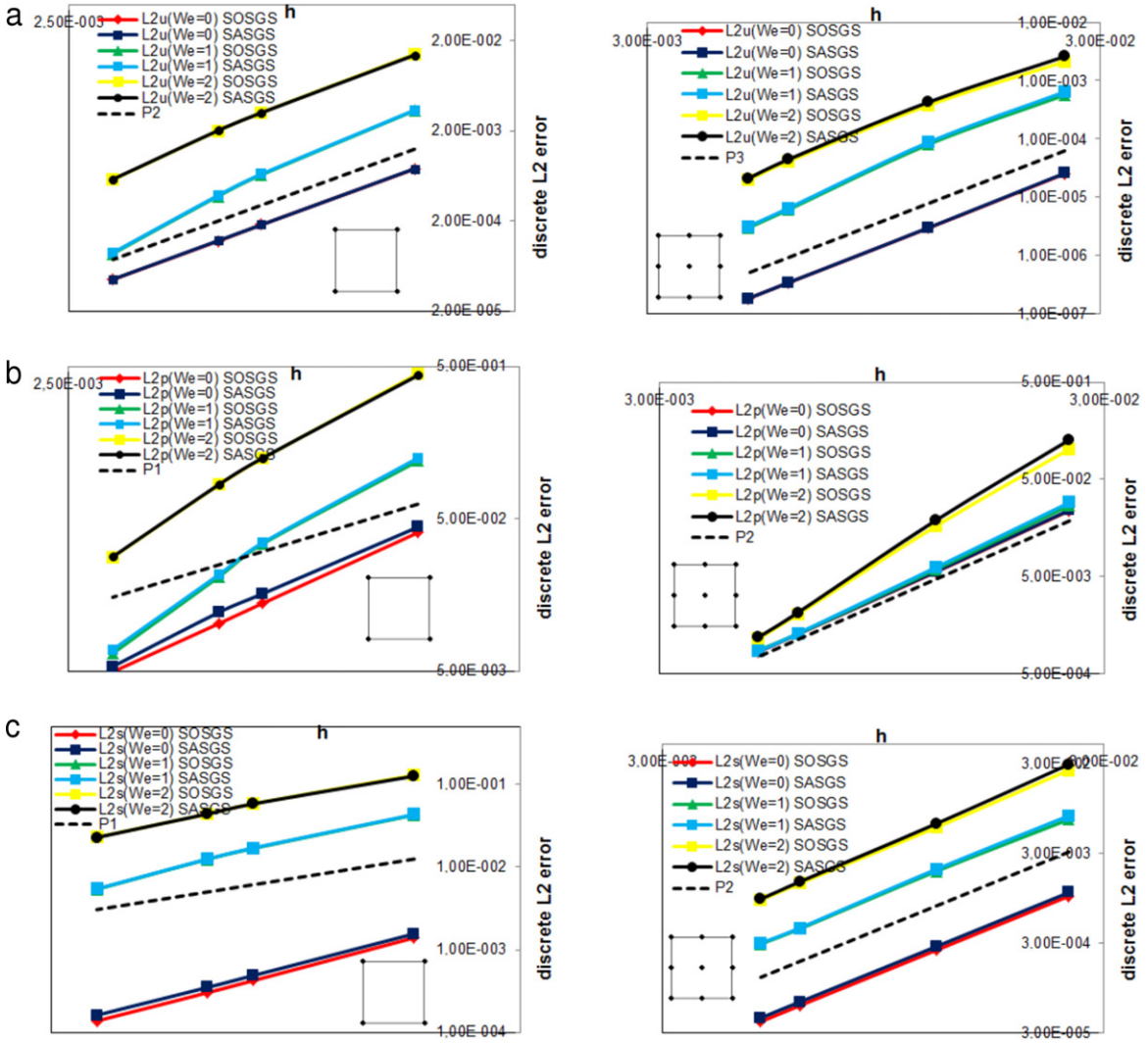

Fig. 1. Discrete L^2errors using Q_1 (left) and Q_2 (right) elements, for the manufactured exact solution. (a) $L^2_{\boldsymbol{u}}$ (velocity error), (b) L^2_p (pressure error) and (c) $L^2_{\boldsymbol{\sigma}}$ (stress error).

problem for We $= 0$, We $= 1.0$ and We $= 2.0$, both for the S-OSGS and the S-ASGS formulations. The Weissenberg number for this case is calculated using the maximum value of the velocity taking the unit side of the computational domain as characteristic length.

The optimal convergence rate expected when the mesh size is reduced using linear elements is two in velocity and one in pressure–elastic stress in the L^2-norm, while using quadratic elements it is three in velocity and two in pressure–stress in the same norm. For both element types the S-OSGS formulation and the S-ASGS formulation show optimal convergence for all fields $\boldsymbol{\sigma}$, $\boldsymbol{u}$ and p.

From the quantitative point of view, if we compare the discrete L^2 errors for the same mesh, the S-OSGS formulation is more accurate that the S-ASGS formulation, showing at least the same error. This is a general trend that we have observed in several numerical examples: the S-OSGS formulation is less dissipative and this leads in general to better accuracy.

4.2. The 4:1 contraction problem

We present in the following the results we have obtained for the classical 4:1 contraction problem in the 2D case. The geometry of the problem is depicted in Fig. 2. Since the problem is symmetric, only half of the domain

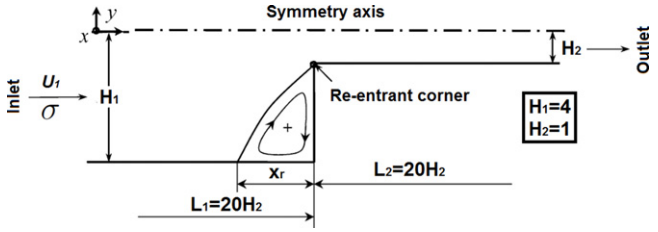

Fig. 2. Geometry description of the two-dimensional 4:1 contraction problem.

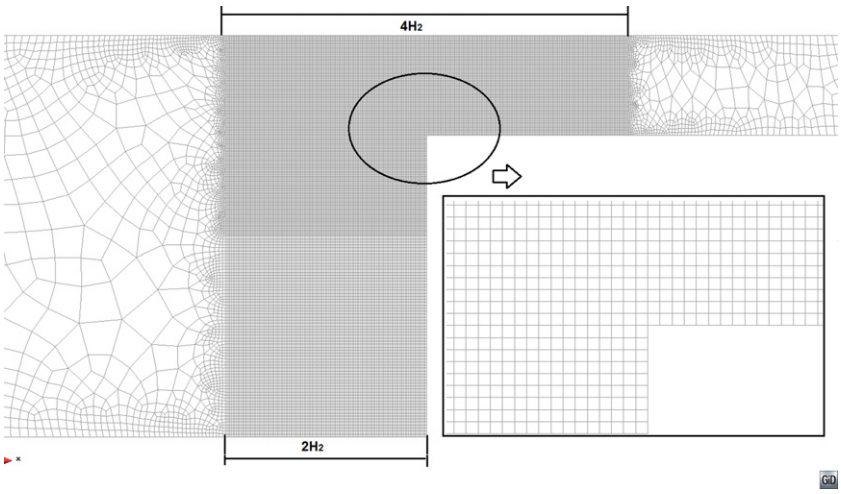

Fig. 3. Typical mesh used in the two-dimensional 4:1 contraction problem.

is considered. To discretize this computational domain we have used finite element meshes that are isotropic in the region surrounding the corner and anisotropic and unstructured further way. One of the meshes used for this problem is shown in Fig. 3.

The characteristic lengths of the problem are detailed in Fig. 2, where in addition we can see the definition of the vortex length X_r used to compare our results with those published by other authors.

Let us describe the boundary conditions of the problem. For the velocity, no-slip conditions are imposed on the solid walls and symmetry conditions are prescribed along the axis $y = 0$, which in this case mean the y-velocity is set to zero. A fully developed parabolic velocity profile and the stress profile associated with the Newtonian behavior are prescribed at the inlet. These are given by

$$u_x = \frac{3Q}{2H_1}\left(1 - \frac{y^2}{H_1^2}\right), \qquad u_y = 0$$

$$\sigma_{xx} = 2\lambda\,(1-\beta)\,\eta_0 \left(\frac{3Q}{H_1^3}y\right)^2, \qquad \sigma_{yy} = 0, \qquad \sigma_{xy} = -\,(1-\beta)\,\eta_0 \left(\frac{3Q}{H_1^3}y\right)$$

where Q is the flow rate, taken as $Q = 1$. As already explained, the boundary conditions for the stresses are required to avoid an excessively large computational domain.

For the outlet, the horizontal velocity is left free, the vertical velocity is taken to be zero and pressure is prescribed to zero, constant. Altogether, the x-component of the normal component of the total Cauchy stress tensor (i.e., the x-component of the boundary traction) is taken to be zero.

We have solved the problem for two different Reynolds numbers (Re $= 1$ and Re $= 0.01$), with a total viscosity of value $\eta_0 = 1$ and with two different values of density ($\rho = 0.01$ and $\rho = 1$, respectively). The parameter β is taken as $\beta = 1/9$ and the relaxation time λ is fixed in terms of the required Weissenberg number. For this example, and using

Table 1
Meshes used in the 4:1 contraction problem.

Q_1	n° elements	n° nodes	$\Delta x_{\min} = \Delta y_{\min}$
M1	27 258	27 667	0.05
M2	39 894	40 501	0.025
M3	105 816	106 671	0.01
Q_2	n° elements	n° nodes	$\Delta x_{\min} = \Delta y_{\min}$
M4	17 573	71 211	0.075
M5	28 859	116 519	0.035

the above definitions, the Weissenberg number is defined in terms of the relaxation time as follows:

$$\mathrm{We} = \frac{\lambda \bar{u}_2}{H_2} = \lambda$$

where $\bar{u}_2$ represents the average velocity at the outflow ($\bar{u}_2 = 1$) and we have taken $H_2 = 1$. The Reynolds number is calculated also using the outflow values, i.e.:

$$\mathrm{Re} = \frac{\rho \bar{u}_2 H_2}{\eta_0} = \rho.$$

To verify the mesh size dependency of the results, we have used three different meshes of bilinear elements (Q_1) and two meshes of biquadratic elements (Q_2). The most significant difference in the results obtained is in the secondary lip vortex that appears in the vertical wall, which is only well captured in the finest mesh.

The most important details of the meshes used are summarized in Table 1. There, $\Delta x_{\min} = \Delta y_{\min}$ is the minimum element size (not node-spacing) in the x- and y-directions, respectively. All the results shown below correspond to mesh M2 for bilinear elements and to mesh M5 for biquadratic elements, unless otherwise indicated.

4.2.1. Oldroyd-B flow at Re = 1

Let us start considering the case with significative inertial effects, i.e., Re = 1. The maximum Weissenberg number that we have been able to reach is We = 5, which is higher than what is usually reported in the literature. For We = 5.5 we have found some instabilities of the iterative scheme, and for We = 6 we have failed to obtain a converged solution. Note that we are considering the stationary problem, and we have attempted to solve it directly. Higher values of the Weissenberg number could probably be reached by integrating in time the transient problem until a steady-state is reached.

Fig. 4 shows distributions of streamlines for all the Weissenberg numbers considered in this case. It is observed that the size of the vortex appearing in the bottom corner decreases as We increases. This is consistent with the results reported in the literature [8,10,33,34].

Using the finest mesh (M3) the secondary lip vortex emerges as We $>$ 2.0. For We $>$ 2.5 it appears clearly defined (both in the M3 and in the M2–M5 meshes) with a bigger size in the more elastic cases. This is perfectly consistent with the results published by Li et al. [8] and the sizes of the vortex are very close to the values reported by Nithiarasu [10].

Fig. 5 shows a comparison of the vortex length obtained as a function of the Weissenberg number with other results that can be found in the literature. The agreement between our results and those presented in the references mentioned in the figure label is good up to We = 2.5, both using bilinear and biquadratic elements. For more elastic cases, i.e. We $>$ 2.5, we did not find results reported in the case Re = 1. From Fig. 5 it is observed that the size of the vortex keeps decreasing as We increases.

Fig. 6 shows a cut line near the contraction corner where pressure is plotted. The contours of pressure and of elastic stress components provided by the proposed formulations for the different Weissenberg numbers analyzed in the case Re = 1 are presented in Figs. 7–10. It is noteworthy that both in the S-ASGS and in the S-OSGS formulations these results are very similar, so that the isolines of the variables are displayed without indicating the formulation employed. The patterns of the results obtained are smooth, without oscillations, and in a good agreement with the results reported in [8,10].

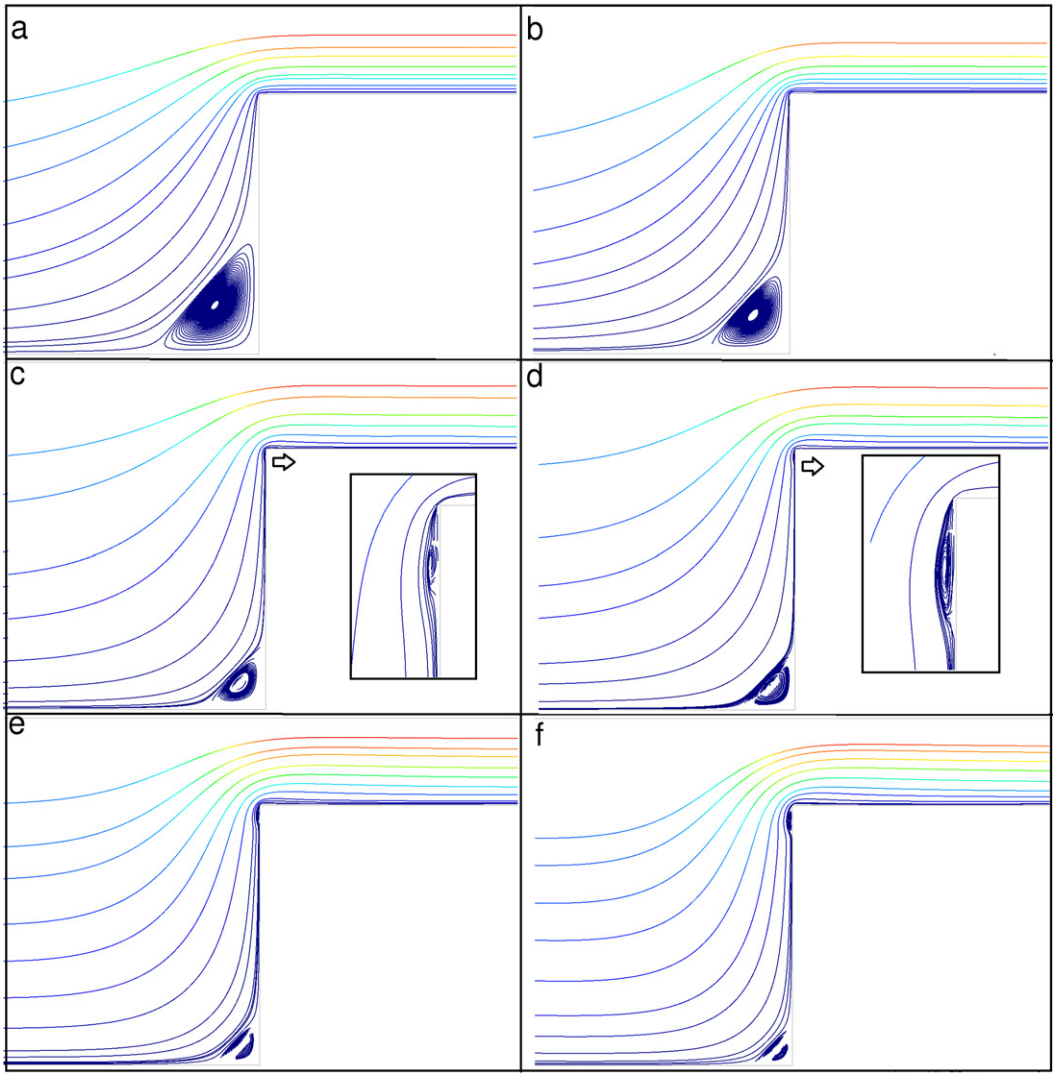

Fig. 4. Close-up view of streamlines near the corner for Re = 1: (a) We = 0, (b) We = 0.5, (c) We = 2.5, (d) We = 3, (e) We = 4 and (f) We = 5.

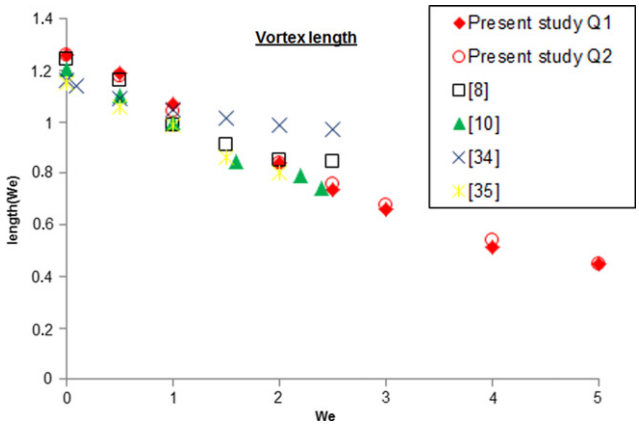

Fig. 5. Vortex size validation at different Weissenberg numbers for Re = 1.

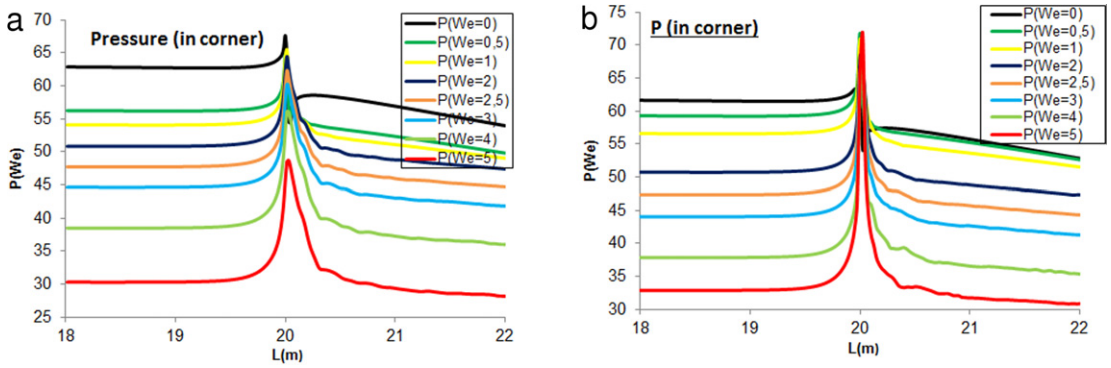

Fig. 6. Pressure in a cut line near the contraction corner for Re = 1: (a) Q_1 elements, (b) Q_2 elements.

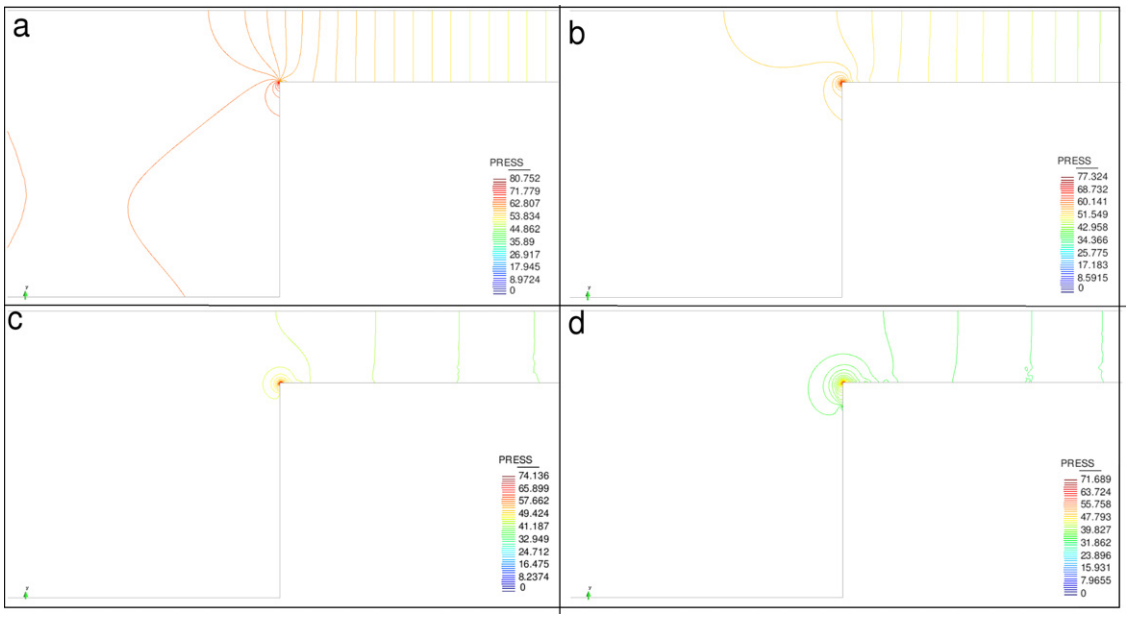

Fig. 7. Pressure isolines near the contraction corner: (a) We = 0, (b) We = 1, (c) We = 3, (d) We = 5.

The elastic stress contours are given in Figs. 8–10. We can note that the elastic stress gradients in the vicinity of the contraction corner are higher with increasing Weissenberg number. The same occurs for the maximum values.

Fig. 11 shows the elastic stress distribution along the horizontal line $y = -1$. It is observed that the peak values of the viscoelastic stresses increase strongly as We increases and no oscillations are observed. We have not encountered any numerical difficulty in capturing it, neither in the nonlinear iterative loop nor in the numerical integration. These values are in accordance with the results presented in [8] (for a proper scaling). Table 2 collects the maximum peak values for each stress component shown in Fig. 6.

To further demonstrate the quality of the results and the absence of oscillations, even in the vicinity of the contraction corner, Fig. 12 shows the horizontal velocity u_x along the symmetry axis $y = 0$ and the vertical velocity u_y along the line $y = -1$, which corresponds to the bottom wall of the narrow region of the domain. The results obtained are in agreement with those reported in [1,35].

4.2.2. Oldroyd-B flow at Re = 0.01

The study of creeping flows in the 4:1 planar contraction problem has proven to be a non-trivial benchmark. In the works of Alves et al. [36,35] the dispersion in the results using different methods of the vortex length was analyzed in detail. In [36], the authors showed that the use of high order schemes (HOS) in a finite volume formulation can

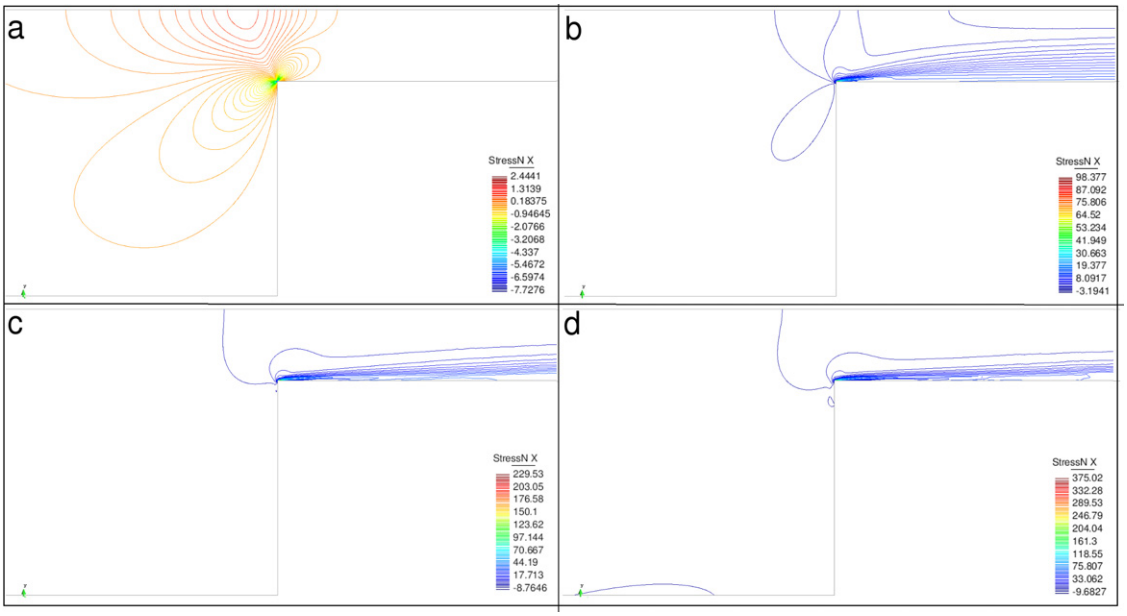

Fig. 8. Normal elastic stress component σ_{xx} near the contraction corner: (a) We $= 0$, (b) We $= 1$, (c) We $= 3$, (d) We $= 5$.

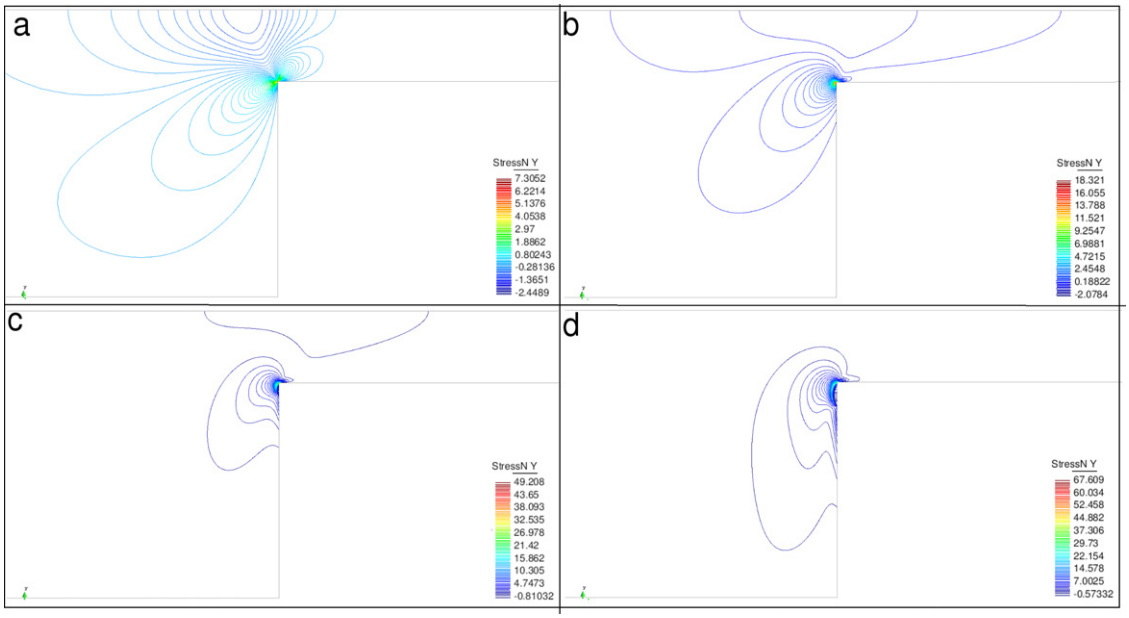

Fig. 9. Normal elastic stress component σ_{yy} near the contraction corner: (a) We $= 0$, (b) We $= 1$, (c) We $= 3$, (d) We $= 5$.

significantly improve the accuracy of the numerical solution in the analysis of viscoelastic flows. They found that the first-order upwind differencing scheme (UDS) is unable to predict accurately the flow pattern in the 4:1 planar contraction even in very fine meshes and for moderate Weissenberg numbers (up to We $= 3.0$). In an exhaustive analysis of the 4:1 benchmark flow using Oldroyd-B and Phan-Thien–Tanner (PTT) fluids, Alves et al. [35] proposed recommended and non-recommended values for the vortex length in creeping flows of viscoelastic fluids. To get an example of wrong values they used a first order UDS and coarse meshes, and for the recommended values they used a successive mesh refinement and a Richardson extrapolation to predict the vortex sizes in conjunction with a high-resolution scheme (MINMOD) to represent the stress derivatives in the constitutive equation. For the

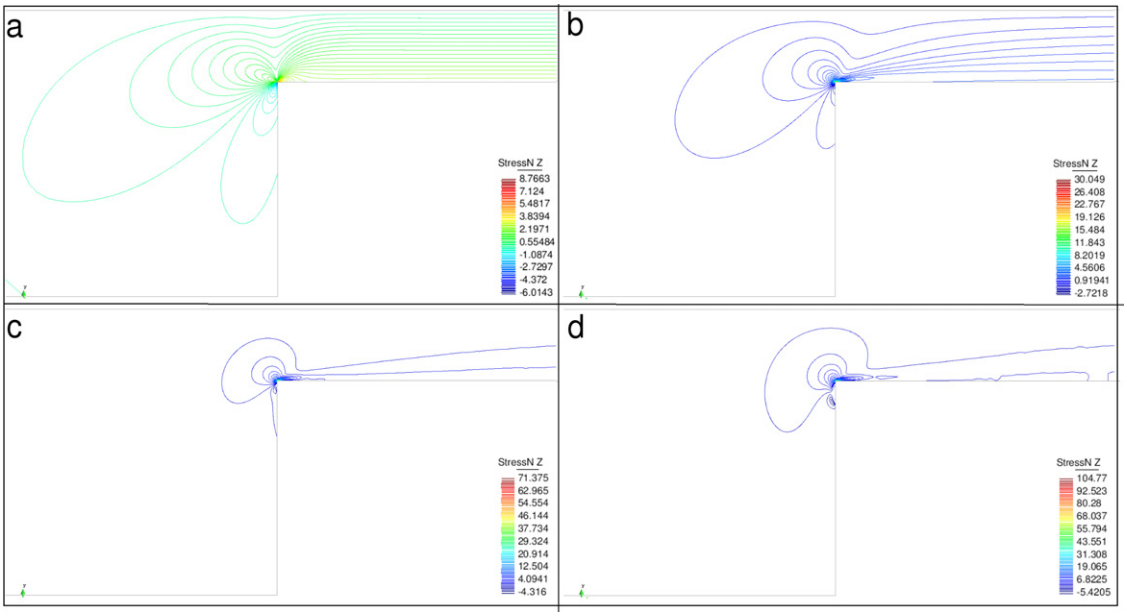

Fig. 10. Elastic stress component σ_{xy} near the contraction corner: (a) We = 0, (b) We = 1, (c) We = 3, (d) We = 5.

Table 2
Maximum peak values for each elastic stress component corresponding to Fig. 6.

We	σ_{xx}	σ_{xy}	σ_{yy}
We = 0.0	7.722	8.766	7.305
We = 0.5	58.174	18.483	12.003
We = 1.0	98.377	30.049	18.321
We = 2.0	162.04	51.16	34.551
We = 2.5	194.6	60.929	41.641
We = 3.0	229.53	71.375	49.208
We = 4.0	301.69	89.128	59.979
We = 5.0	375.02	104.77	67.609

non-recommended case, the authors obtained a decrease in the vortex size with increasing Weissenberg number up to We = 1.5, and an increase in the size for more elastic cases. However, for the recommended results, the decrease of the vortex length remains up to We = 3.0 (the most elastic case that the authors could solve).

As it can be seen from the studies of Sato and Richardson [34] and Matallah et al. [37], the solutions for the Oldroyd-B fluid with Re = 0.01 in the 4:1 planar contraction flow problem are almost identical to those for the non-inertial or creeping flow case (Re = 0), so in the comparison we use both cases to validate our results.

Fig. 13 shows the comparison of the vortex length distribution in terms of the Weissenberg number. These results show the behavior recommended by [35] (with a four times coarser mesh in our case), and are in agreement with the results published by [36,38,39] up to We = 5 which is the highest elastic value for which we could find results reported for this case, even though we could reach We = 6.5 with our formulations.

The stress distribution patterns for Re = 0.01 are very similar to those of the Re = 1 case, and therefore not repeated here. Only the streamlines are shown in Fig. 14 to compare them with the results of other authors. In the Re = 1 case, the secondary lip vortex appears for We > 2. However, for Re = 0.01, this secondary vortex is already clearly defined for We = 2. This value is comparable to those found in [8,10], although the Weissenberg number at which the vortex appears is clearly mesh-dependent.

The final result that we present for the case Re = 0.01 is intended to demonstrate the benefits of using a DC technique as the one proposed in this paper. In the example we are considering, when the elasticity of the fluid is increased,

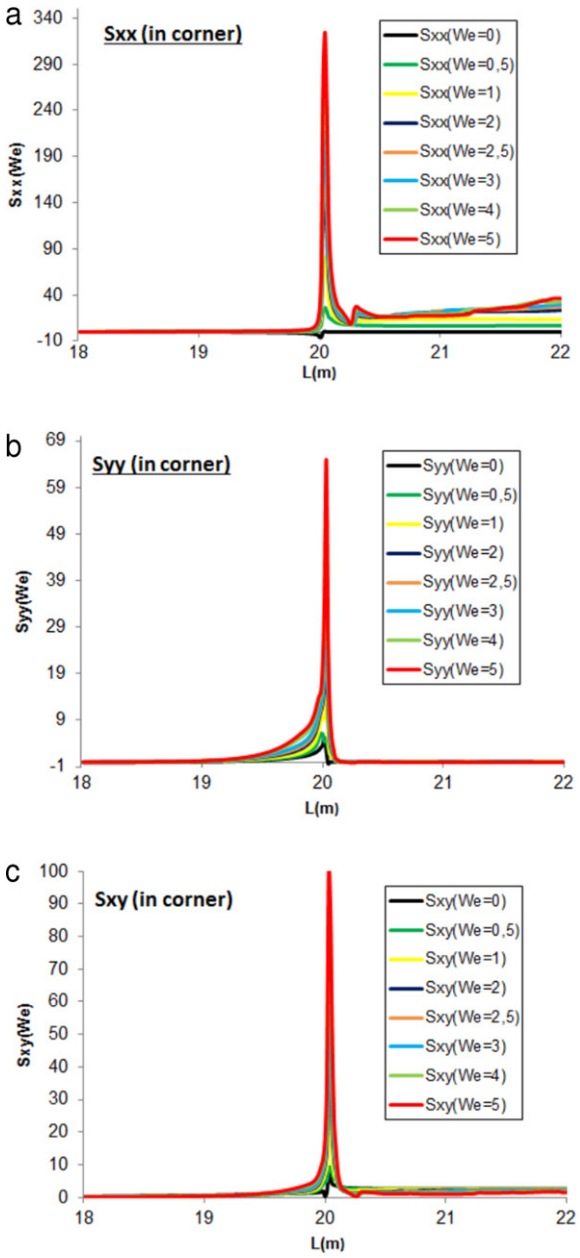

Fig. 11. Elastic stress components along the horizontal line $y = -1$ for Re $= 1$: (a) σ_{xx}, (b) σ_{yy}, (c) σ_{xy}.

the elastic stress gradients in the vicinity of the contraction corner are higher the higher the Weissenberg number is. If the finite element mesh is not fine enough to resolve these gradients, node-to-node oscillations may appear. Fig. 15 shows an example of these oscillations in a stress component, and how they are corrected when the DC technique is used. The curve shown corresponds to the σ_{yy} stress component along $y = -1$ computed with a Weissenberg number We $= 3$ using mesh M1, but the same behavior is observed in all cases where there is a peak in one of the unknowns.

4.2.3. Some results for Re $= 0.01$ *and for* Re $= 1$

As for the primary vortex, we can show the length variation for the secondary vortex. For this case, we have not found results reported in the literature against which we could compare our results. From Fig. 16 it is seen that

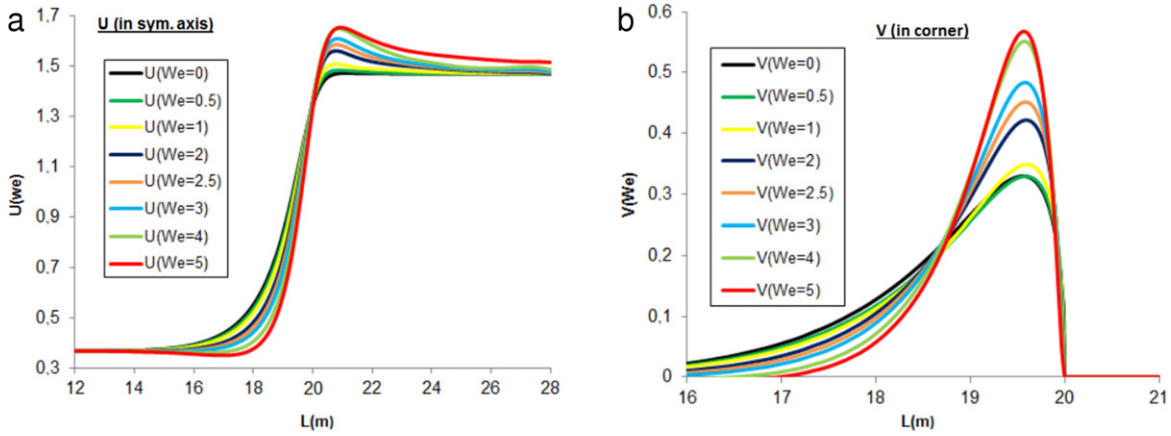

Fig. 12. Velocity profiles: (a) u_x along $y = 0$ (symmetry axis), (b) u_y along $y = -1$ (bottom wall of the narrow region).

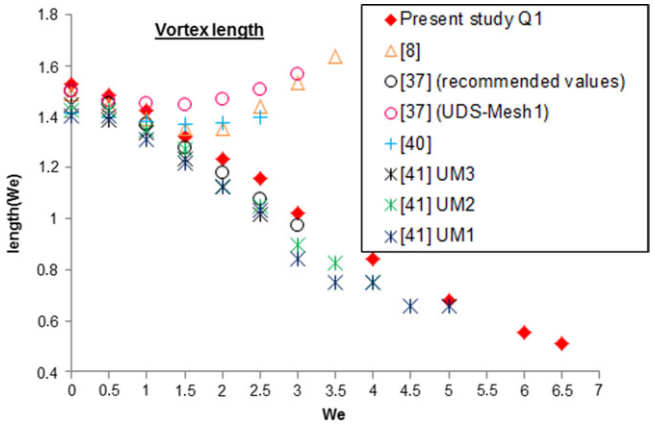

Fig. 13. Vortex size validation at different Weissenberg numbers for Re = 0.01.

the growth in the vortex size with the Weissenberg number is smooth. We show there both the results obtained for Re = 0.01 and for Re = 1.

Table 3 shows the pressure drop ($\Delta p = p_{\text{inlet}} - p_{\text{outlet}}$) for all the Weissenberg numbers analyzed. As we can see, Δp is very similar using bilinear and biquadratic elements, even though the pressure peak is better captured by the biquadratic elements. Both in the inertial (Re = 1) and in the quasi non-inertial (Re = 0.01) cases, we can see that Δp decreases when the Weissenberg number is increased, which is what is expected from the physical point of view. In viscoelastic flows the velocity profile is more blunt than for Newtonian fluids, and the pressure drop increases much less rapidly with the mass flow rate than in the Newtonian case. This is why polymers, which provide elasticity to the fluid, are often used as *drag-reducing agents* [40].

4.3. A tridimensional example

To show that the formulation proposed in this paper can be applied to the 3D case without any difficulty, we extend the 4:1 contraction problem of the previous subsection to three dimensions. The problem geometry is shown in Fig. 17, and the mesh to discretize it is shown in Fig. 18. It is an unstructured mesh composed of 528 396 linear tetrahedral elements and 98 814 nodes.

The $y = 0$ and $z = 0$ planes (see Fig. 18) are considered to be symmetry planes, and thus the normal velocity to these planes is set to zero. The domain of Fig. 17 can be considered one fourth of the flow domain. In the same way as for the 2D case, the half-width of the shorter square channel, $H_2 = 1$, is taken as the characteristic length scale and

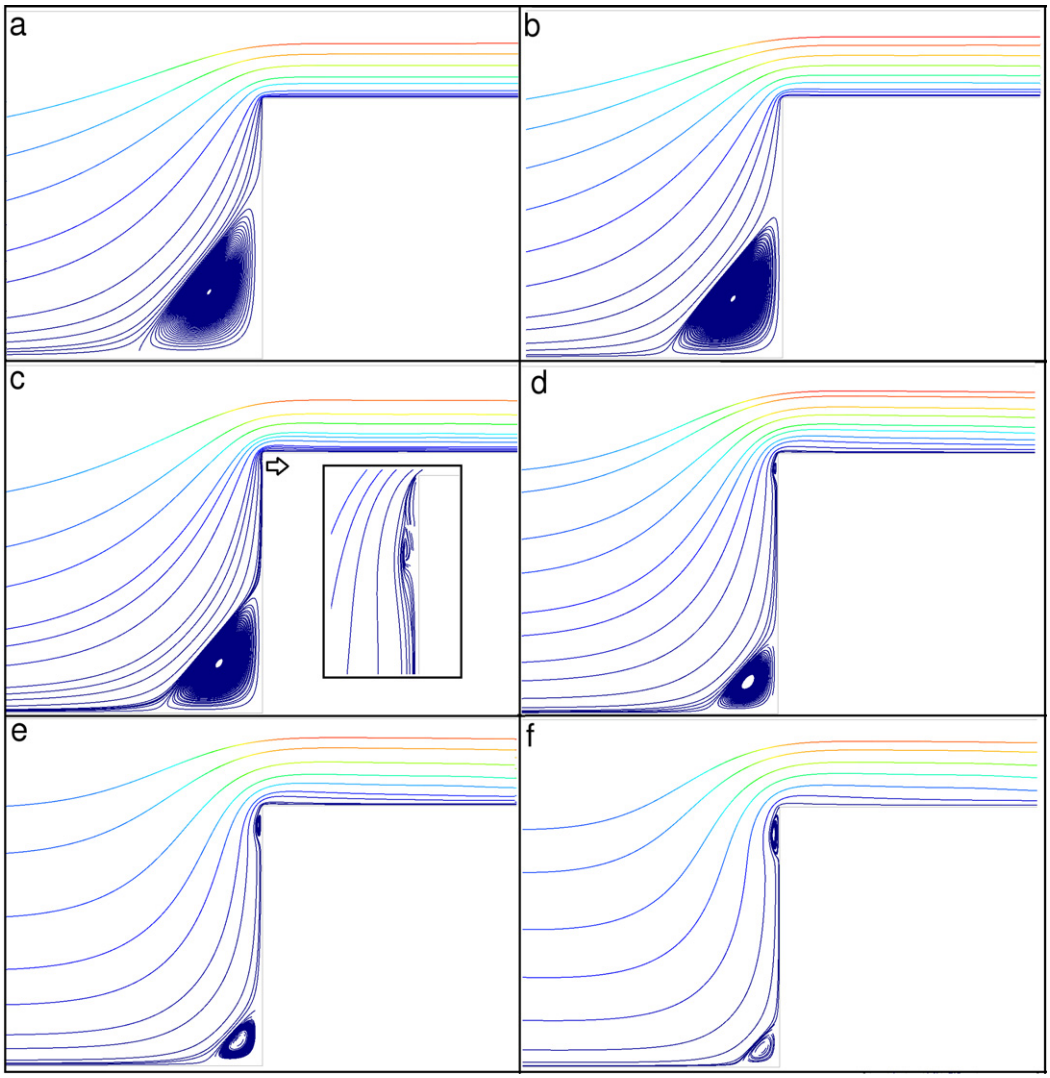

Fig. 14. Close-up view of streamlines near the corner for Re = 0.01: (a) We = 0, (b) We = 1, (c) We = 2, (d) We = 4, (e) We = 5, (f) We = 6.5.

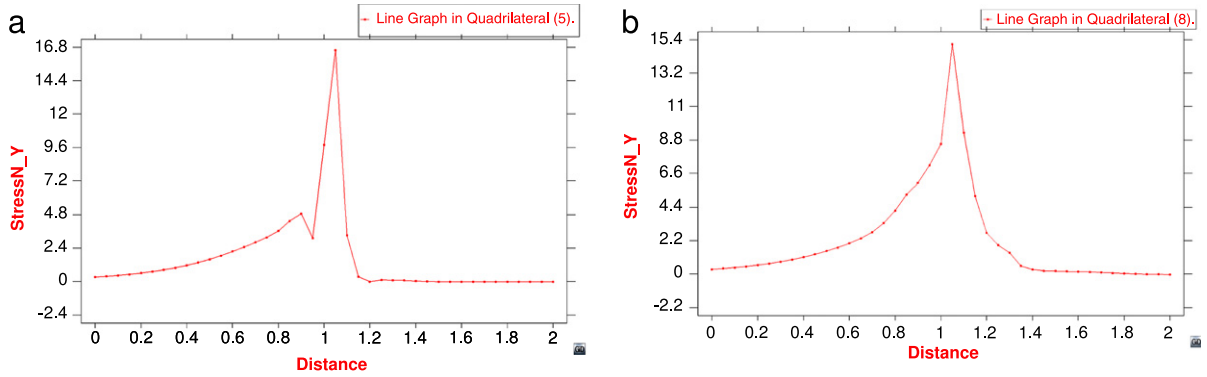

Fig. 15. Typical oscillation in a stress component: (a) without discontinuity capturing technique, and (b) with discontinuity capturing technique.

the average velocity in that channel $\bar{u}_2 = 1$ is the characteristic velocity scale. The boundary conditions employed are the straightforward extension of those used in the 2D case.

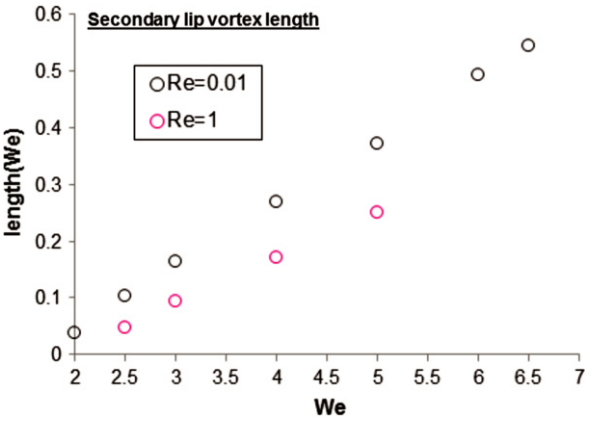

Fig. 16. Secondary vortex size at different Weissenberg numbers for Re = 0.01 and Re = 1.

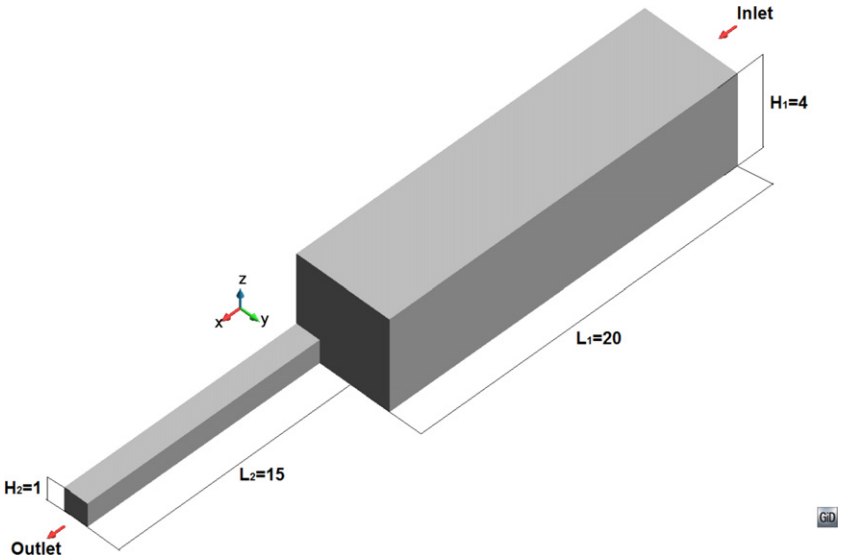

Fig. 17. Sketch of the 3D 4:1 contraction problem.

Table 3
Pressure drop for different Weissenberg and Reynolds numbers using bilinear (Q_1) and biquadratic (Q_2) elements.

Re = 1	Δp (Q_1)	Δp (Q_2)	Re = 0.01	Δp (Q_1)
We = 0	63.793	62.539	We = 0	63.067
We = 0.5	58.69	60.47	We = 0.5	60.449
We = 1.0	56.05	57.78	We = 1.0	57.124
We = 2.0	52.198	52.12	We = 2.0	50.414
We = 2.5	48.252	48.539	We = 2.5	47.158
We = 3.0	45.207	45.637	We = 3.0	43.994
We = 4.0	42.166	41.294	We = 4.0	38.648
We = 5.0	37.52	37.22	We = 5.0	33.934
–	–	–	We = 6.0	29.842
			We = 6.5	29.236

The discrete and linearized problem is solved by using an iterative solver based on the BiCGStab (Stabilized version of BiConjugate Gradient Squared) method of van der Vorst [41], with the additive Schwarz preconditioner.

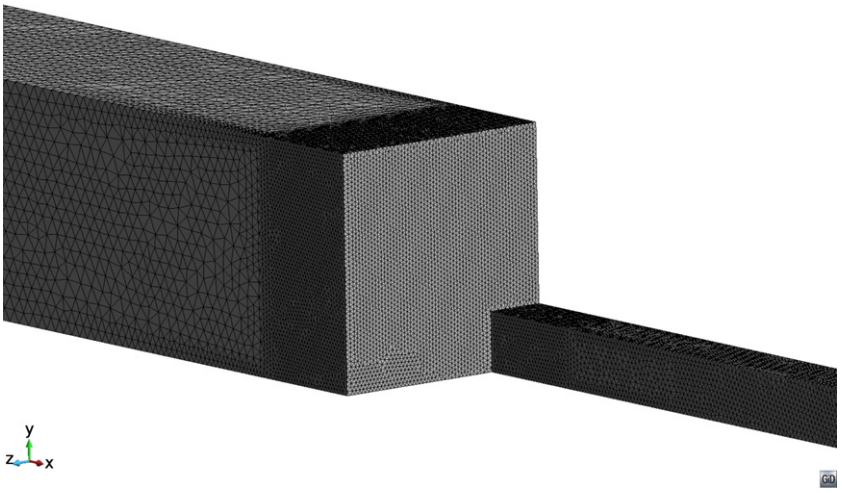

Fig. 18. Mesh used in the 3D 4:1 contraction problem.

As for the 2D case, the constitutive model is Oldroyd-B. The dimensionless numbers that govern the problem have been taken $\mathrm{Re} = 0.01$ and $\mathrm{We} = 1$. Higher values of the Weissenberg number would require finer meshes, particularly when the secondary lip vortex appears. However, it is not our purpose in this example to analyze complex physics, but only to assess the feasibility of the 3D extension of the formulation.

Some streamlines are shown in 19. A general isometric view is depicted in Fig. 19(a), whereas two cuts with perpendicular planes are shown in Fig. 19(b). The primary vortex can be clearly appreciated, as well as the emergence of the secondary lip vortex. From Fig. 19(b) it is also observed that the solution develops a symmetry with respect to the plane $y = z$. Three-dimensional flow patterns can also be clearly observed.

Fig. 20 shows the contours of the two transversal velocity components u_y and u_z in two perpendicular planes $y = 0.5$ and $z = 0.5$, both parallel to the symmetry axis $y = z = 0$. Note that, despite having a non-structured mesh, the results show the symmetry of the problem.

One of the most difficult results to obtain in a problem with an abrupt change in geometry is the pressure field. Fig. 21 shows the pressure contour lines around the corner zone (Fig. 21(a)), and the pressure variation along a cut line on the wall in one of the symmetry planes in the contraction zone (Fig. 21(b)). In both cases we can see that no oscillations appear, and the solution is smooth. If we compare the pressure variation along a line in the corner between the 2D case (Fig. 6) and the 3D case (Fig. 21(b)), we can appreciate that the rate at which pressure diminishes after the corner peak is greater in the latter.

Both in the 2D and in 3D cases DC techniques need to be used to avoid node-to-node oscillations in the elastic stress components. Fig. 22 shows the variation of the σ_{zz} component across the corner in the line $y = 0.5$, $z = 0.5$ without (Fig. 22(a)) and with (Fig. 22(b)) the introduction of the DC dissipation. The spurious secondary peak observed in the first case is removed by the introduction of the DC term, even if the solution in Fig. 22(b) is not perfectly smooth. Note that the mesh used in the calculation is rather coarse for the complexity of the problem being solved.

5. Conclusions

In this paper we have introduced stabilized finite element methods for the viscoelastic flow problem based on the VMS concept. Starting from residual-based formulation for the momentum and the continuity equations, we have moved to the use of a split orthogonal sub-grid scale technique for them. This is not a residual based stabilization, but introduces stabilization for pressure, stress and velocity in independent terms. We have observed a better behavior of this approach in regions where the solution displays high gradients. For the approximation of the constitutive equation, classical residual-based stabilization works well.

The method finally designed allows one to obtain globally stable solutions using equal interpolation for all the unknowns and to treat convection-dominated problems. However, node-to-node oscillations in the viscoelastic stress components and the pressure in regions of high gradients still remain. A discontinuity-capturing technique has been introduced to remove them.

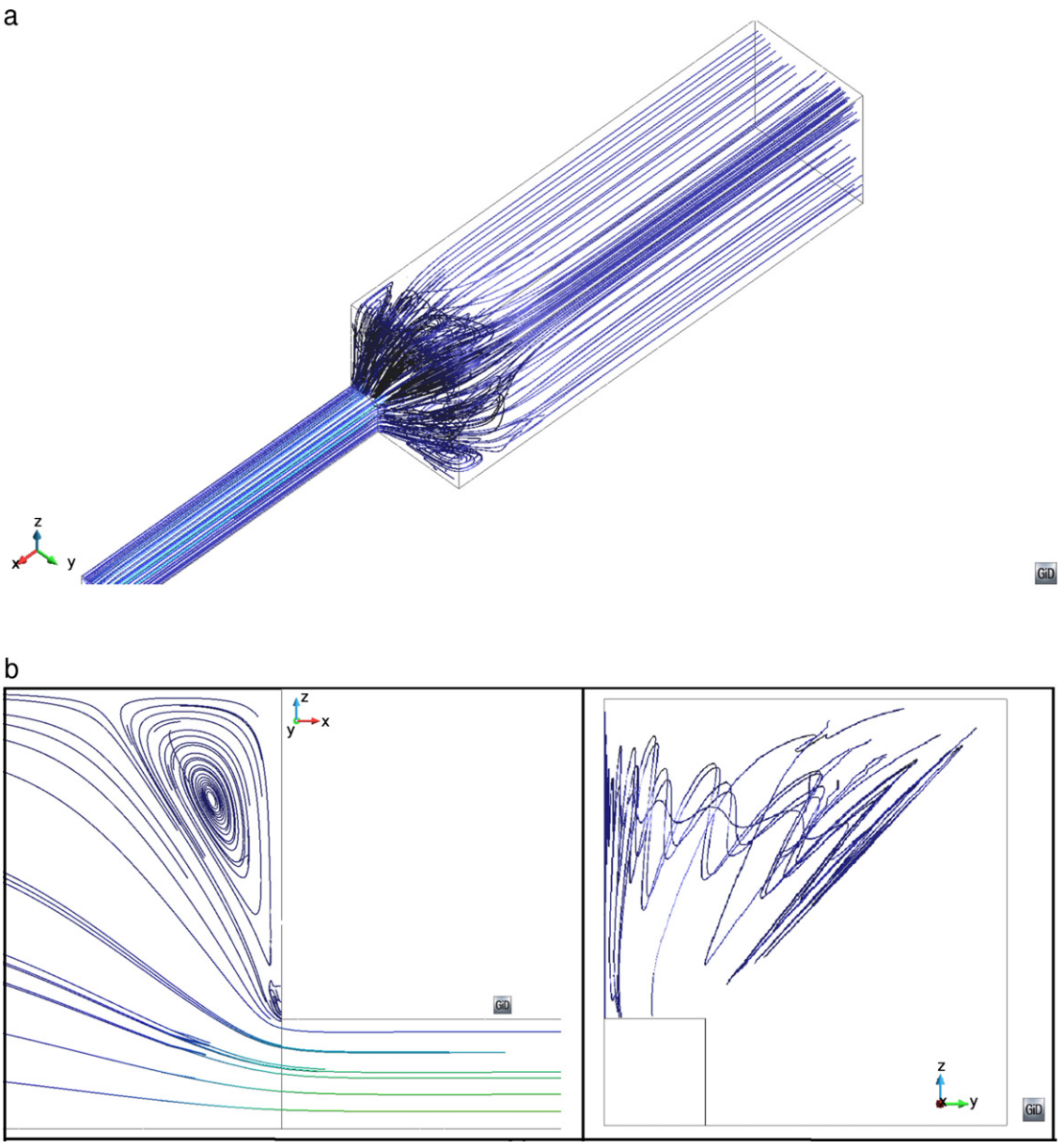

Fig. 19. Streamlines in the 3D 4:1 contraction problem (Re $=$ 0.01 and We $=$ 1): (a) Isometric view. (b) Cuts with the planes $y = 0$ (left) and a plane $x =$ constant close to the contraction plane (right).

The resulting formulation is accurate, showing optimal convergence properties for smooth solutions, and robust, able to deal with high gradients of the unknowns appearing at corners in viscoelastic flow problems. We have presented here the results obtained for a simple manufactured solution and for the 4:1 contraction problem, both in the classical 2D version and in a 3D extension. An indication of the robustness of the formulation is that we have been able to solve problems with Weissenberg numbers significantly higher than those reported in the literature we have consulted, even solving directly the stationary problem.

Acknowledgments

E. Castillo gratefully acknowledges the support received from CONICYT (Programa de Formación de Capital Humano Avanzado/Becas-Chile Folio 72120080), and from the Universidad de Santiago de Chile. R. Codina

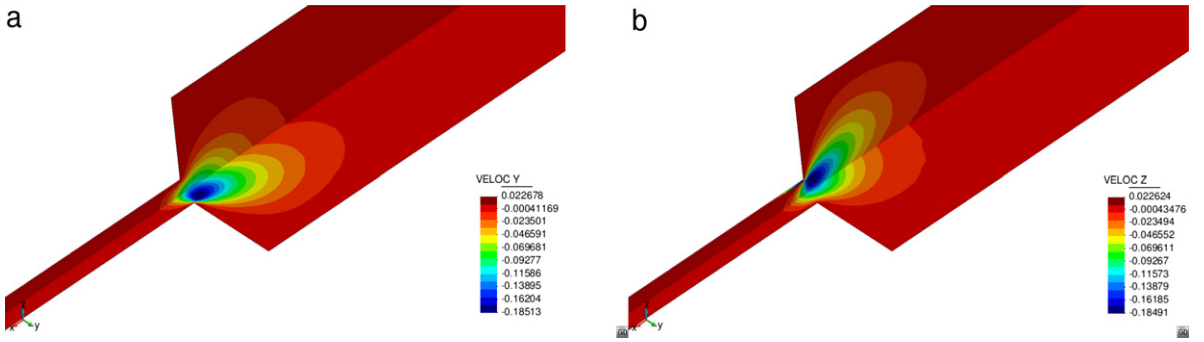

Fig. 20. Contours of transversal velocity components on the planes $y = 0.5$ and $z = 0.5$: (a) u_y, (b) u_z.

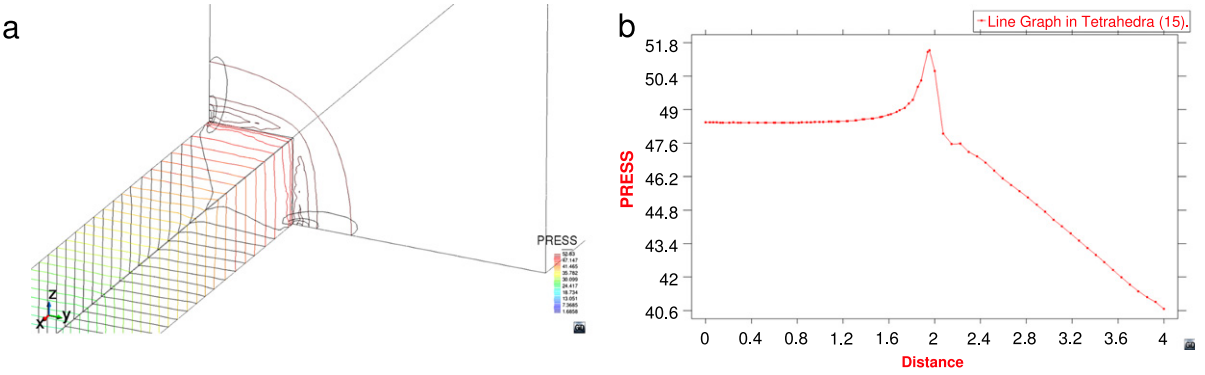

Fig. 21. Pressure around the corner: (a) contour lines, (b) along a cut line across the corner.

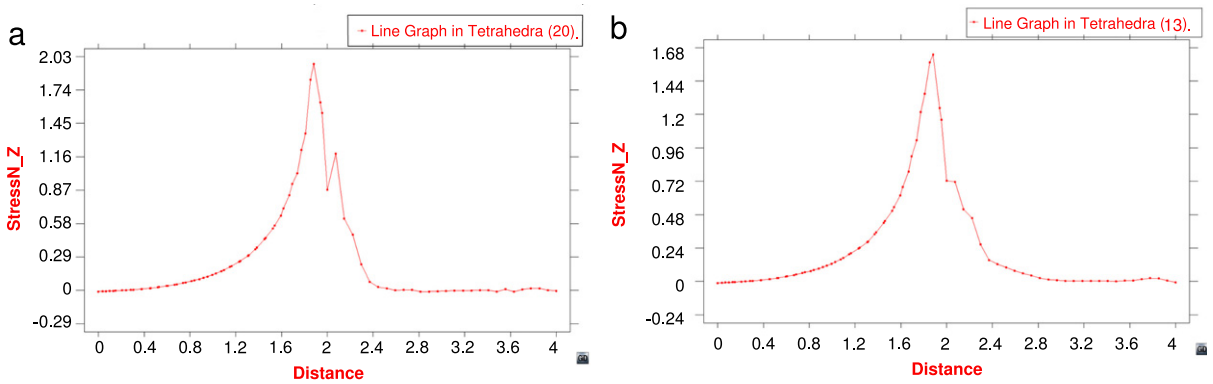

Fig. 22. Normal elastic stress component σ_{zz} across the corner: (a) without discontinuity-capturing technique, and (b) with discontinuity-capturing technique.

gratefully acknowledges the support received from the Catalan Government through the ICREA Acadèmia Research Program.

References

[1] H.-C. Lee, A nonlinear weighted least-squares finite element method for the Oldroyd-B viscoelastic flow, Appl. Math. Comput. 219 (1) (2012) 421–434. Towards a Computational Interpretation of Physical Theories Towards a Computational Interpretation of Physical Theories.
[2] J. Kwack, A. Masud, A three-field formulation for incompressible viscoelastic fluids, Internat. J. Engrg. Sci. 48 (11) (2010) 1413–1432. Special Issue in Honor of K.R. Rajagopal.
[3] D. Sandri, Numerical study of a new finite element method for the approximation of viscoelastic fluid flow problems, J. Non-Newton. Fluid Mech. 118 (2–3) (2004) 103–120.

[4] A.N. Brooks, T.J. Hughes, Streamline Upwind/Petrov–Galerkin formulations for convection dominated flows with particular emphasis on the incompressible Navier–Stokes equations, Comput. Methods Appl. Mech. Engrg. 32 (1–3) (1982) 199–259.
[5] J. Marchal, M. Crochet, A new mixed finite element for calculating viscoelastic flow, J. Non-Newton. Fluid Mech. 26 (1) (1987) 77–114.
[6] Y. Fan, R. Tanner, N. Phan-Thien, Galerkin/least-square finite-element methods for steady viscoelastic flows, J. Non-Newton. Fluid Mech. 84 (2–3) (1999) 233–256.
[7] O.M. Coronado, D. Arora, M. Behr, M. Pasquali, Four-field Galerkin/least-squares formulation for viscoelastic fluids, J. Non-Newton. Fluid Mech. 140 (1–3) (2006) 132–144.
[8] X. Li, X. Han, X. Wang, Numerical modeling of viscoelastic flows using equal low-order finite elements, Comput. Methods Appl. Mech. Engrg. 199 (9–12) (2010) 570–581.
[9] O. Zienkiewicz, R. Codina, A general algorithm for compressible and incompressible flow—part I. The split, characteristic-based scheme, Internat. J. Numer. Methods Fluids 20 (1995) 869–885.
[10] P. Nithiarasu, A fully explicit characteristic based split CBS scheme for viscoelastic flow calculations, Internat. J. Numer. Methods Engrg. 60 (5) (2004) 949–978.
[11] E. Carew, P. Townsend, M. Webster, On a discontinuity capturing technique for Oldroyd-B fluids, J. Non-Newton. Fluid Mech. 51 (2) (1994) 231–238.
[12] R. Codina, A discontinuity-capturing crosswind-dissipation for the finite element solution of the convection–diffusion equation, Comput. Methods Appl. Mech. Engrg. 110 (3–4) (1993) 325–342.
[13] P. Nithiarasu, O. Zienkiewicz, B.S. Sai, K. Morgan, R. Codina, M. Vazquez, Shock capturing viscosities for the general fluid mechanics algorithm, Internat. J. Numer. Methods Fluids 28 (1998) 1325–1353.
[14] J. Bonvin, M. Picasso, R. Stenberg, GLS and EVSS methods for a three-field Stokes problem arising from viscoelastic flows, Comput. Methods Appl. Mech. Engrg. 190 (29–30) (2001) 3893–3914.
[15] D. Sandri, On a FEM method for a linearized version of the Oldroyd's problem, Comput. Methods Appl. Mech. Engrg. 191 (44) (2002) 5045–5065.
[16] F. Brezzi, M. Fortin, Variational formulations and finite element methods, in: F. Brezzi, M. Fortin (Eds.), Mixed and Hybrid Finite Element Methods, in: Springer Series in Computational Mathematics, vol. 15, Springer, New York, 1991, pp. 1–35.
[17] M. Fortin, R. Pierre, On the convergence of the mixed method of Crochet and Marchal for viscoelastic flows, Comput. Methods Appl. Mech. Engrg. 73 (3) (1989) 341–350.
[18] A.C. Bogaerds, W.M. Verbeeten, G.W. Peters, F.P. Baaijens, 3D viscoelastic analysis of a polymer solution in a complex flow, Comput. Methods Appl. Mech. Engrg. 180 (3–4) (1999) 413–430.
[19] F.P. Baaijens, Mixed finite element methods for viscoelastic flow analysis: a review, J. Non-Newton. Fluid Mech. 79 (2–3) (1998) 361–385.
[20] T.J. Hughes, G.R. Feijóo, L. Mazzei, J.-B. Quincy, The variational multiscale method—a paradigm for computational mechanics, Comput. Methods Appl. Mech. Engrg. 166 (1–2) (1998) 3–24.
[21] R. Codina, Stabilization of incompressibility and convection through orthogonal sub-scales in finite element methods, Comput. Methods Appl. Mech. Engrg. 190 (13–14) (2000) 1579–1599.
[22] R.B. Bird, R.C. Amstrong, O. Hassager, Dynamics of Polymeric Liquids, Vol. 1: Fluid Mechanics, second ed., Wiley, New York, 1987.
[23] R.B. Bird, C.F. Curtiss, R.C. Amstrong, O. Hassager, Dynamics of Polymeric Liquids, Vol. 2: Kinetic Theory, second ed., Wiley, New York, 1987.
[24] E. Fernández-Cara, F. Guillén, R. Ortega, Mathematical modeling and analysis of viscoelastic fluids of the Oldroyd kind, in: Handbook of Numerical Analysis, VIII, North-Holland, 2002.
[25] R. Codina, Finite element approximation of the three-field formulation of the Stokes problem using arbitrary interpolations, SIAM J. Numer. Anal. 47 (1) (2009) 699–718.
[26] E. Castillo, R. Codina, Stabilized stress–velocity–pressure finite element formulations of the Navier–Stokes problem for fluids with nonlinear viscosity, Comput. Methods Appl. Mech. Engrg. 279 (2014) 554–578.
[27] R. Codina, A stabilized finite element method for generalized stationary incompressible flows, Comput. Methods Appl. Mech. Engrg. 190 (2001) 2681–2706.
[28] R. Codina, Analysis of a stabilized finite element approximation of the oseen equations using orthogonal subscales, Appl. Numer. Math. 58 (3) (2008) 264–283.
[29] R. Becker, M. Braack, A finite element pressure gradient stabilization for the Stokes equations based on local projections, Calcolo 38 (2001) 173–199.
[30] G. Matthies, P. Skrzypacz, L. Tobiska, A unified convergence analysis for local projection stabilisations applied to the Oseen problem, ESAIM Math. Model. Numer. Anal. 41 (2007) 713–742.
[31] S. Badia, On stabilized finite element methods based on the Scott–Zhang projector. Circumventing the inf–sup condition for the Stokes problem, Comput. Methods Appl. Mech. Engrg. 247–248 (2012) 65–72.
[32] R. Guénette, M. Fortin, A new mixed finite element method for computing viscoelastic flows, J. Non-Newton. Fluid Mech. 60 (1995) 27–52.
[33] T. Phillips, A. Williams, Viscoelastic flow through a planar contraction using a semi-Lagrangian finite volume method, J. Non-Newton. Fluid Mech. 87 (2–3) (1999) 215–246.
[34] T. Sato, S.M. Richardson, Explicit numerical simulation of time-dependent viscoelastic flow problems by a finite element/finite volume method, J. Non-Newton. Fluid Mech. 51 (3) (1994) 249–275.
[35] M.A. Alves, P.J. Oliveira, F.T. Pinho, Benchmark solutions for the flow of Oldroyd-B and PTT fluids in planar contractions, J. Non-Newton. Fluid Mech. 110 (1) (2003) 45–75.
[36] M. Alves, F. Pinho, P. Oliveira, Effect of a high-resolution differencing scheme on finite-volume predictions of viscoelastic flows, J. Non-Newton. Fluid Mech. 93 (2–3) (2000) 287–314.
[37] H. Matallah, P. Townsend, M. Webster, Recovery and stress-splitting schemes for viscoelastic flows, J. Non-Newton. Fluid Mech. 75 (2–3) (1998) 139–166.

[38] M. Aboubacar, M. Webster, A cell-vertex finite volume/element method on triangles for abrupt contraction viscoelastic flows, J. Non-Newton. Fluid Mech. 98 (2–3) (2001) 83–106.
[39] J.M. Kim, C. Kim, J.H. Kim, C. Chung, K.H. Ahn, S.J. Lee, High-resolution finite element simulation of 4:1 planar contraction flow of viscoelastic fluid, J. Non-Newton. Fluid Mech. 129 (1) (2005) 23–37.
[40] R.B. Bird, W.E. Stewart, E.N. Lightfoot, Transport Phenomena, second ed., John Wiley & Sons, Ltd., 2007.
[41] H.A. van der Vorst, BI-CGSTAB: a fast and smoothly converging variant of BI-CG for the solution of nonsymmetric linear systems, SIAM J. Sci. Stat. Comput. 13 (1992) 631–644.